LEVEL II

⑫

STANFORD/NASA AMES JOINT INSTITUTE FOR SURFACE AND MICROSTRUCTURE RESEARCH
DEPARTMENT OF MATERIALS SCIENCE AND ENGINEERING
STANFORD UNIVERSITY
STANFORD, CA 94305

FABRICATION AND PROPERTIES OF MULTILAYER STRUCTURES

prepared by

W. A. Tiller
T. W. Barbee, Jr.

April 1981   SU-DMS-81-R-4

DTIC
ELECTE
JUN8 1981
S   D
D

Third Semiannual Technical Report for Period 1 September 1980 - 28 February 1981

prepared for

COPY

Department of MATERIALS SCIENCE AND ENGINEERING

STANFORD UNIVERSITY

81 6 08 065

SU-DMS-81-R-4

THIRD

SEMIANNUAL TECHNICAL REPORT

ON

FABRICATION AND PROPERTIES OF

MULTILAYER STRUCTURES

1 September 1980 - 28 February 1981

Stanford/NASA Ames Joint Institute for Surface and Microstructure Research

Department of Materials Science and Engineering

Stanford University, Stanford, CA 94305

DTIC
ELECTE
S
JUN8 1981
D

D

REPORT DOCUMENTATION PAGE	READ INSTRUCTIONS BEFORE COMPLETING FORM

1. REPORT NUMBER	2. GOVT ACCESSION NO.	3. RECIPIENT'S CATALOG NUMBER
SU-DMS-81-R-4	AD-A099793	

4. TITLE (and Subtitle)	5. TYPE OF REPORT & PERIOD COVERED
FABRICATION AND PROPERTIES OF MULTILAYER STRUCTURES	3rd Semiannual Technical Report (9/1/80 - 2/28/81) no. 3 1 Sep 80 28 Feb 81
	6. PERFORMING ORG. REPORT NUMBER

7. AUTHOR(s)	8. CONTRACT OR GRANT NUMBER(s)
W. A. Tiller T. W. Barbee, Jr. L. Nagel K. Seaward W. Dibble Y. T. Thathachari	MDA903-79-C-0484, ARPA Order-3706

9. PERFORMING ORGANIZATION NAME AND ADDRESS	10. PROGRAM ELEMENT, PROJECT, TASK AREA & WORK UNIT NUMBERS
Stanford/NASA Ames Joint Institute for Surface and Microstructure Research, Department of Materials Sci. & Engrg. Stanford University, Stanford, CA 94305	

11. CONTROLLING OFFICE NAME AND ADDRESS	12. REPORT DATE
Advanced Research Projects Agency (ARPA) 1400 Wilson Blvd. Arlington, VA 22209	Apr 1981
	13. NUMBER OF PAGES
	60

14. MONITORING AGENCY NAME & ADDRESS(if different from Controlling Office)	15. SECURITY CLASS. (of this report)
	Unclassified
	15a. DECLASSIFICATION/DOWNGRADING SCHEDULE

16. DISTRIBUTION STATEMENT (of this Report)

Unlimited Distribution

17. DISTRIBUTION STATEMENT (of the abstract entered in Block 20, if different from Report)

18. SUPPLEMENTARY NOTES This contract is awarded under Basic Agreement N00014-79-H-0029, dated 81 September 79, amended by modification P00001 and P00002, issued by the Office of Naval Research. This research is sponsored by Defense Advanced Research Project Agency (DARPA)

19. KEY WORDS (Continue on reverse side if necessary and identify by block number)

REACTIVE SPUTTERING, FILM FORMATION, SILICON DIOXIDE, SILICON CARBIDE, SEMI-CONDUCTOR PROCESSING, THERMAL OXIDATION, INTERSTITIAL SPECIES, CRYSTALLOGRAPHY, MOLECULAR ORIBTALS, AMORPHOUS FILMS, INTEGRATE CIRCUITS

20. ABSTRACT (Continue on reverse side if necessary and identify by block number)

The program has as its goal the development of vapor deposition processes for application to integrated circuit technology. Its purpose is to investigate vapor deposition techniques that offer potential for synthesis of materials having new, unique structures and/or of higher quality than currently attainable. Technological application of these materials will be a significant

DD FORM 1473 EDITION OF 1 NOV 65 IS OBSOLETE
1 JAN 73
S/N 0102-LF-014-6601

332575

consideration in the selection of specific systems for study, particularly multilayer integrated circuit applications.

In this period, experiments with the new cryopumped system were performed. Reactive sputtering research focused on a detailed study of SiO_x and a more broad guage study of MO_x films for a number of metals M (M $\equiv$ Si, W, Aℓ, Zn, Zr, Mg) on 3" diameter wafers. High deposition rates, a wide range of stoichiometry and either amorphous or crystalline films were formed. The cleanliness of the new system is orders of magnitude better than the old system. Multiple source deposition studies focused on SiC_x formation. X-ray analysis, refractive index and bandgap data all confirm the formation of SiC films. Good control of the sputter deposition of these films has been demonstrated.

In the theoretical area, the constraints placed on closed n-ring assemblies (Si_nO_{3n}) in SiO_2 are being assessed to identify those constraints which differentiate the structure between the crystalline and vitreous forms. Interactions between various interstitial species and dimer (Si_2O_7) units or tetramer (Si_4O_{12}) rings in silica have been carried out using CNDO/2. Great progress has been made in evaluating the total energy, E_T, at 0^oK for the following interstitial species, Si, Si^{2+}, 0, $0^=$, 0^{2+}, 0_2, H_2O, OH^- and H^+.

INTRODUCTION

During this third six-month period of the program, the experimental emphasis focused on reactive sputtering of a variety of oxides with continued in-depth study on SiO_x plus continued work on the two-source deposition of SiC_x films. In all areas, meaningful progress has been made and it is especially significant to see how well these techniques can be extended to other oxide materials. The theoretical emphasis continued on both the structural and the energetic aspects of the SiO_x material and significant gains are reported in those sections of this report.

A. Experimental Results

1. Reactive Sputtering

(a) SiO_x

In the previous report[1], some experimental evidence indicated that oxygen introduced into the chamber at the substrate surface was back-diffusing to the silicon sputtering source and contaminating the surface. In addition, CV plot data suggested that hydrocarbon contamination was present in the SiO_x films.

During the present period, construction was completed on a sputtering system designed to deposit uniform films on 3" diameter substrates (see Fig. 1a). This system provides several advantages over the one described in previous reports. Specifically:

(1) A helium cryopump has eliminated the problem of hydrocarbon contamination which resulted from back-diffusion of oil in the previous system.

(2) The increased pumping speed of this system allows for controlled-stoichiometry syntheses at a much lower reactive gas/argon ratio, which

reduces the previous tendency toward target oxidation at high O_2 pressure.

(3) An oxygen dispersion ring (see Fig. 1b) further isolated the target from the reactive gas while providing a uniform, radially symmetric flow of oxygen to the substrate surface.

(4) The use of a 3" target has increased the area of film uniformity. The system illustrated in Fig. 1a will support a target up to 6" diameter, should this become necessary.

Electron microprobe analysis has confirmed our anticipatd correlation of refractive index with stoichiometry by coinciding with previously measured SIPOS films (see Fig. 2). this implies that low temperature fabrication produces films with a microstructural integrity at least equal to that found with the high temperature CVD process.

The present emphasis is on determining the optimum combination of sputtering parameters (e.g., Si deposition rate, oxygen pressure, argon pressure) which will produce maximum film uniformity. Since uniformity is affected by the nature of the oxygen flow over the substrate, it is important to have a wide effective range of oxygen pressure available for a particular synthesis. Fortunately, there is a well behaved relationship between gas pressure, sputtering rate and resulting oxide stoichiometry. Figure 3 illustrates a typical experiment in which oxygen pressure and RF power are varied independently to cover a full stoichiometric range. At 500 W, we note that the film stoichiometry varies linearly with P_{O_2} so that the film stoichiometry can be simply changed by changing P_{O_2}. Likewise, at constant P_{O_2}, the film stoichiometry can be simply changed by changing the sputter power.

The radial symmetry of our present samples allows film uniformity to be easily checked using ellipsometric techniques and continued improvement is being made in this area. To illustrate the film uniformity in the new system, Fig. 4 indicates results obtained on an $SiO_{1.5}$ film. We note that the index of refraction, n_f , is quite uniform out to a 1" radius from the center of the wafer and then falls off seriously at $\sim 0.25"$ from the outer periphery of the wafer. Over this same film distance, the wafer thickness is found to be constant within $\sim 15\%$. The next step, here, will be to optimize the position of the oxygen flow relative to the substrate surface, thus allowing a much more uniform oxygen incidence rate.

Procedures have now been established for routinely measuring electrical properties of each of our samples. Monitoring the resistance and capacitance-diode characteristics will ensure that the oxide layers are passivating and that the interface integrity is uniform. These measurements will lead directly to the more thorough evaluation of film electrical behavior (A.C.) planned for the future.

(b) Extension to Other Oxide Systems

During this period, a series of exploratory experiments into the synthesis of the oxides of aluminum, zirconium, magnesium, and zinc were performed. the purpose of these experiments was to determine: (1) Can this process be applied to other oxide systems? (2) What characteristics in the synthesis of these other oxides differ from those of SiO_x. (3) Do the results suggest that this process can be applied to the synthesis of other compounds; i.e., to those containing N, C, Cℓ , F, etc? (4) What are the limitations of this process? In the following, the results of these experiments will be outlined and a short summary included.

-3-

The results of these experiments are summarized in Table I. It was found possible to synthesize oxides of all materials attempted except magnesium, where difficulties with the sputtering target limited the experiments. Only two of the materials deposited were found to form crystalline films under the conditions explored (zinc and zirconium). ZnO was formed with control of stoichiometry and conductivity. ZrO_2 was stabilized in the high temperature cubic form, with an apparently amorphous phase appearing as the oxide was reduced by synthesis at lower oxygen pressures. All other films were amorphous as formed.

Also included in this table are the heats of decomposition, ΔH, of these materials at ambient conditions and ϕ, the ratio of the molecular volumes of the oxides to that of their metallic components in their elemental forms.

$A\ell O_x$

Experiments on synthesis of $A\ell O_x$ are summarized in Table II. Both the $A\ell$ deposition rate and the oxygen pressure were systematically varied. It was observed that all films formed were non-stoichiometric and amorphous (x-ray diffraction analysis). Composition was determined by electron microprobe analysis for samples 197 and 199. the refractive index of 199 was $n_f \simeq 2.0$ from standard ellipsometric observations. This is somewhat larger than $\alpha - A\ell_2O_3$ but consistent with a higher aluminum concentration. Sample 197 was examined by electron microprobe analysis on a radius of the sample; these results are shown in Fig. 5. Note that near stoichiometric oxide is present near the edge of the sample where the aluminum deposition rate is smallest. Also, a transition from clear to translucent brown was observed for $O/A\ell$ ratios less than approximately 1.25. This may be associated with color centers or aluminum clusters resulting in Mie scattering and absorption.

-4-

The variation in oxygen to aluminum ratio with position on a radius of the sample can be interpreted as resulting from the spatial variation in the incidence rate of aluminum atoms with position, which is characteristic of the magnetron sputter deposition source used. If one assumes that the oxygen incidence rate is constant over the sample surface and that the sticking coefficient or reaction rate is uniform, the thickness profile of the aluminum can be unfolded from these data. This assumption requires that the number of oxygen atoms incorporated into the film is constant and independent of position on the substrate. The thickness of aluminum, therefore, varies in ratio from 1.0 at 10 mm from the sample center to 0.8 at 20 mm and 0.7 at 30 mm. This thickness variation is in general agreement with the expected deposition profile of the aluminum, implying that the oxygen gas distribution is sufficiently uniform for synthesis of uniform composition films if the aluminum incidence rate is constant.

These results also demonstrate that the stoichiometry of the deposited films can be systematically varied over a broad range by control of the rates of incidence of the oxygen and aluminum. the stoichiometry is a sensitive function of the relative rates of incidence requiring control of this parameter if uniform films are to be deposited.

Possible application of this process may center on the use of these films as passivation layers on III-V compounds, as well as unique passivation layers for more exotic materials.

ZrO_x

Synthesis process parameters for Zr/O films are tabulated in Table III. All films were deposited onto Si(100) single crystal substrates. Analysis was

performed using standard powder x-ray diffractometry, electron microprobe analysis and ellipsometry.

The zirconium deposition rate was maintained constant in these experiments while the oxygen pressure varied by a factor of four. In all cases, the films were near stoichiometric ZrO_2. The film formed at the lowest oxygen pressure showed a slight deviation from stoichiometry. All films were observed to be fine-grain polycrystalline, having the cubic structure ($a_0 = 5.01$ A, FCC). This cubic structure is not expectd at room temperature, the equilibrium form being monoclinic. The cubic form is generally only observed at temperatures above $\sim 2300^0$C in equilibrium and thus represents a true metastable state. Samples formed at lower oxygen pressures also showed indications of a broad shallow diffraction maxima which could be associated with either an amorphous component or the multiplicity of diffraction peaks associated with orthorhombic structure ZrO_2.

The observation of a high reactivity of oxygen with the zirconium, as evidenced by the insensitivity of the film structure to oxygen pressure, is consistent with the common use of zirconium and titanium as oxygen getters. The crystallinity of the deposition product and the cubic structures are unique and indicate that material specific to oxygen sensor applications can be deposited in thin film form.

ZnO_x

Synthesis process parameters for Zn/O films are tabulated in Table IV. All films were deposited on Si(100) single crystal substrates. Analysis was performed using x-ray powder diffractometry, ellipsometry and simple conductivity tests.

In all cases the films were observed to have the hexagonal crystalline structure expected for ZnO. Preliminary measurements of the lattice parameter as a function of position showed no dependence upon location on the substrate and therefore on stoichiometry of the film. Film electrical resistance varied with radial position from the center of the sample to the edge, as shown in Fig. 6. The electrical resistivity of ZnO_x is a function of stoichiometry as reflected in these results. Film composition is yet to be characterized by electron microprobe analysis.

These results demonstrate that the modified experimental apparatus allows synthesis of oxides of controllable stoichiometry of elements such as Zn, a very high sputtering rate material having a very stable oxide. Possible applications include transparent conducting films for windows and for solar cell contacts. It is important to note that these films were deposited onto room temperature substrates which were isolated from the sputtering plasma. These are important characteristics for many possible applications of this material.

Summary

The experimental results presented in the preceding discussion demonstrate the general applicability of the synthesis technique used for the formation of SiO_x films. This process allows the synthesis of whole new classes of materials onto electronic device materials which can be expected to act as passivating layers or active components in the device. Formation of oxide film onto room temperature substrates at deposition rates of 5 A/sec (18,000 A/hr) with control of stoichiometry and, in some cases, of the crystalline structure, represents a unique capability. This processing method makes possible the synthesis of materials which have not previously been

accessible to the micro electronics community for evaluation as device components. In addition, it can be used to synthesize SiO_x films onto substrates held at low temperatures so that VLSI structures may be fabricated with minimum thermal history.

2. Synthesis of SiC_x Films by Two-Source Deposition

There is a high level of interest in the semiconductor device possibilities of β-SiC , the cubic form. the temptation to generate SiC by a process compatible with silicon technology has directed this part of the program toward low temperature (< 1000^{0}C) deposition of SiC by sputtering. The system used has a combination of state-of-the-art features for sputter deposition: magnetron sources (plasma decoupled from the deposition surface), substrate heater, cyro-pumped chamber, and single, dual or triple-source arrangement, parallel or at various angle to the substrate/deposition surface. The goal is to achieve deposition of large areas of single crystal β-SiC by a sputtering technique at a temperature with typical silicon processing temperatures.

The set of experiments described here indicates that Si can be deposited on Si or Al_2O_3 by co-sputtering silicon and carbon targets. SiC films having a preferred orientation were formed at 700^{0}C on Al_2O_3 and at 750^{0}C on Si substrates. In addition to investigating the structure of the films, various SiC film properties have been measured. The refractive index, band gap, and stoichiometry were evaluated using standard techniques. These analyses will be described. The present experiments are a continuation of the dual-source depositions described in the previous semi-annual report[1]. Deposition reproducibility has been established and the various analyses of the SiC indicate that β-SiC has been formed. The next set of experiments will

involve a sputtering configuration that should enhance the surface mobility of Si and C, resulting in SiC films of greater crystalline perfection. This configuration and existing supporting data will be described in the section on future direction.

Sputter Deposition of SiC

First the sputtering configuration and deposition parameters will be reviewed. In Fig. 7 a schematic is given of the arrangement inside the sputtering chamber. Two sources were employed; a graphite source was operated in tne DC mode and a single crystal silicon source was operated in the RF mode. The source-to-source separation was 16.5 cm. The substrate could be heated up to 850°C by means of a heat-shielded quartz lamp configured so that the substrate was heated from the back surface. The source-to-substrate distance was 10-15 cm. The combination of the magnetron sources and this large source-to-substrate distance were considered sufficient to keep the sputtering plasma from influencing the reaction at the substrate surface.

Before initiating the plasma, the sputtering chamber was pumped down to 2×10^{-6} Torr. A plasma was maintained with 4 microns (4×10^{-6} Torr) of Argon. As indicated in Fig. 7, a monotonically varying distribution of sputtered material is expected from each target. With the targets facing directly downwards, their surfaces parallel to the substrate surface, an overlap of the Si and C distributions is evident so that the entire range of SiC_x is deposited on the substrate. One end of the deposition is carbon-rich, the other end is silicon-rich, and stoichiometric SiC is somewhere in between.

Two types of substrates were used, Si and $A\ell_2O_3$. The Si was device-quartz (100) 20Ω-cm p-type Si which had been cleaned by the industry-standard "RCA clean"; this leaves a reproducible (amorphous) oxide film on the silicon

surface. The Al_2O_3 was SOS-quality sapphire, polished on the side used for
deposition, and cleaned the same way as the silicon. The Al_2O_3 is not
considered to have any type of amorphous film on its surface and should act as
a single-crystal deposition surface.

Analysis of SiC Films

As explained at the end of the sputter deposition section, there is a
calculable distribution of sputtered material from each target. Thus, the
deposition thickness as a function of location on the substrate can be
anticipated given the experimental sputtering rates of the targets.
Calculations were made for the SiC depositions and an example was given in the
last semi-annual report [1] (see pages 10-11, Table IV, and Fig. 9). Briefly
summarizing what has been observed, the experimental and calculated thickness
profiles agreed very well. Where there was a deviation between theory and
experiment, the film was no longer SiC, but consisted of SiC imbedded in
polycrystalline silicon, as verified by X-ray diffractometry. Once this was
accounted for, agreement was obtained over the entire deposition range.

A number of SiC depositions were made and the highlights are listed in
Table V. The structure of the films was deduced by X-ray diffractometry and
by using an X-ray Read camera which is similar to Debye-Scherrer/Laue but
optimized for thin films. The X-ray analysis, resulting in what is called
preferred orientation, produced only the 111 (and higher order) reflections of
β-SiC. The refractive index of the films was measured by ellipsiometry. Near
the stoichiometric region the value was 2.6, agreeing with the literature
value.

Film composition was assessed by both electron microprobe and by Auger
analysis and good agreement was found for the two techniques. Composition

-10-

profiles for Si and C are shown in Fig. 8. By varying the power on the Si target, the stoichiometric SiC location could be moved,as indicated in the figure. The Auger analysis has produced noteworthy results on the Si and C line shapes and how the line shapes are influenced by the various environments of the Si and the C produced by the variable-composition depositions.

For the SiC deposited on Al_2O_3 ,optical measurements could be made. Preliminary measurements of the transmitted intensity are shown in Fig. 9. The bandgap evaluated by this approximate method is about 3 eV, which is the bandgap expected for SiC.

Future Direction

Further investigation of the material properties of the described SiC deposition is underway. A more exacting analysis is being performed to compute the bandgap from the optical data. The depositions will be scrutinized by SEM and TEM to establish grain size and growth morphology. Electrical propertis of the film will be measured, particularly resistivity and carrier type.

As mentioned in the motivation section, a new set of experiments is planned to investigate a surface mobility-enhancement effect. First, a change from dual to single source deposition of SiC will be attempted to simplify the evaluation of the mobility-enhancement effect. The single source is powdered α-SiC compressed into a disk shape. Experimentally, the mobility enhancement consists of co-sputtering a material that is immiscible with both the substrate and the SiC (Sn is a candidate), while the substrate is maintained above the melting temperature of the immiscible material. This idea is shown schematically for a dual source deposition in Fig. 10. What is envisioned is that a liquid-like film of the inert material will form a 2D array (liquid

-11-

lattice idea) just above the substrate. This inert array will enhance the surface mobility of the sputtered species (Si and C) (i) by perhaps guiding the sputtered material to preferred sites for epitaxial film growth, or (ii) by being in the liquid state and thereby allowing higher surface mobility than the solid substrate would allow. The effect of mobility enhancement has been called the liquid-like film effect (LLFE).

A mobility enhancement of the type described (the mechanism as presented is presently fictitious) has been seen for the Cu-Pb system and for other systems as well. Referring to Fig. 11, as the Pb vapor pressure is increased, the surface diffusivity (directly related to the surface mobility) of copper is increased. Because these data are available, another set of experiments is planned in parallel with the SiC + Sn depositions. A model system consisting of a simpler deposition reaction will be investigated. At present, two possible model systems to test the LLFE are Cu sputtered in a Pb environment and W sputtered in a Sn environment.

B.   Theoretical Results

In present atomistic modeling of the thermal oxidation of silicon, [3-5], the structure of the near interface region is of crucial concern because this is a key determining factor in the formation of fixed oxide charge and of interface charge states during the oxidation process. Although the transition of Si to vitreous SiO_2 may be favored to proceed via a crystalline α-cristobalite buffer layer containing Si-interstitial defects[5], the subsequent internal oxidation of these Si_I defects leads to swelling stresses which distort the lattice structure to a vitreous structure of a very similar density. An understanding of this important transition and of the residual defects stored in this non-stoichiometric buffer layer

requires an understanding of the differences between crystalline and vitreous SiO_2 on an atomistic level. Such understanding may lead to ultimate controllable reduction in the magnitudes of the fixed oxide charge, Q_f, and in the density of interface charge states, N_{it}.

The thin non-stoichiometric interface region existing during thermal oxidation is expected to be closely analogous to bulk SiO_x films formed during reactive sputtering of silicon or by the SIPOS process. Thus, to properly deal with this class of structures, one needs understanding not only of the crystalline SiO_2/vitreous SiO_2 transition but also of the structural consequences associated with the introduction of SiO_n species into the network and interstitial spaces of the SiO_2. It is expected that this will aid in understanding the roles of $C\ell$, H, N and various annealing atmospheres on the structure and electrical properties of SiO_x and SiO_2 films.

To understand the formation and properties of SiO_x films, it is essential to know the structure of these films at an atomic level, the spatial mechanism involved in the formation of these structures and the energetics of these structures. Since direct experimental data are not currently available, recourse must be made to theoretical models. Our theoretical approach involves two steps: (1) modeling of vitreous SiO_2 relative to crystalline SiO_2 and (2) modeling vitreous SiO_x structures relative to vitreous SiO_2. The overall problem has been divided into a sequence of simpler tasks, some of which have been completed while others are in progress.

(1) Modeling of Amorphous Silica

The current models of vitreous silica are not sufficiently detailed for the goals envisioned, thus, a different approach has been taken. We partition the description into primary building block considerations, dimer unit considerations and ring structure considerations. Via this path, one is able

-13-

to generate any possible macroscopic structure be it crystalline or vitreous, be it stoichiometric or non-stoichiometric and one is more able to understand the atomic scale defects.

(a) Basic Units

All silica structures, crystalline or vitreous, are made up of the same basic units - oxygen tetrahedra with a silicon interstitial. Adjacent tetrahedra are linked by the sharing of a corner referred to as the bridging oxygen. In perfect silica, all the corners of the tetrahedra are bridging oxygens. In real silica, some of these bridging oxygens will have moved into interstitial positions leaving vacancies at these sites. Thus, the description of any silica structure essentially involves describing the relative orientation of every pair of adjacent linked tetrahedra which we will refer to as the dimer unit.

The tetrahedra are the least variable units in the silica structures and practically retain their shape and dimensions in most silicas, even when subject to large pressures. This view is reinforced by noting that the free energy of formation of SiO_2 at room temperature is 212 kcal/mole whereas the free energy difference between any two silica structures is only $\sim$ 2-4 kcal/mole[6]. Thus, ~99% of the free energy storage resides in the tetrahedral units.

The tetrahedra are almost perfectly regular as illustrated in Fig. 12. The six edges are nearly equal (2.65 ± 0.10 A); the four corners are at nearly the same distance from the central Si (1.62 ± 0.05 A). Thus, the O-Si-O angles are about 110 ± 10⁰. The small deviations from regularity and the small variations in shape and dimensions of the tetrahedra in different silica structures should be considered as second order effects. These are evidently due to the different environments of the unit in different

directions and to the non-uniform forces present. We will ignore these small variations in our initial considerations.

A scheme for linking the tetrahedra into a macroscopic structure is illustrated in Fig. 13. We start with a single tetrahedron (#1) and we link it to four others as first nearest neighbours (2,3,4 and 5) by defining the three angular parameters specifying each dimer (1-2; 1-3; etc.). Each of these four unis can then be linked to three new units leading to 12 second nearest neighbours. This procedure can be continued until an adequate volume of the structure has been built. In order for this procedure to be manageable and meaningful, restrictive criteria and classifying procedures are necessary. There is no general reason to expect the environment of any unit in any given structure to be vastly different from that of another in the same structure. Thus, it should be adequate to define only a few dimers in a sample volume. For most crystalline silica structures, defining a single dimer unit and a few symmetry rules has been shown to be sufficient to build the entire structure to a good approximation [7]

(b) Dimer Unit

Figure 14 illustrates how the three angles $(\theta, \delta_1, \delta_2)$ defining a dimer unit can be chosen. The angle θ is made by the two silicons at the bridging oxygen. The angles δ_1, δ_2 are the two dihedral angles defining the position of one oxygen from each of the two tetrahedra, O_1 and O_2 respectively, relative to the $Si_1 - O_0 - Si_2$ plane. Since the size and shape of the tetrahedra are known, the other four oxygens are automatically fixed and the dimer is fully defined by ϕ, δ_1 and δ_2 . The dihedral angles defining O_3 and O_4 can be expected to be about $\delta_1 \pm 120^0$. Similarly O_5 and O_6 are defined by dihedral angles $= \delta_2 \pm 120^0$.

-15-

The bridge angle θ is generally found to be close to 144^0 in most crystalline silica[8]. The current models of amorphous SiO_2 are based on wire models, [9], sometimes relaxed by computer simulation, which assume a distribution of θ from 120^0 to 180^0 with a maximum at 144^0 and random values of Si_1 and Si_2. However, the range of θ in vitreous SiO_2 is probably much less than the assumed range of 120^0-180^0. In very early data on high cristobalite, θ was assumed to be 180^0 but recent determinations of $\theta \sim 144^0$ [10,11]. Many investigators still use the old incorrect value. Data on high tridymite show a similar shift in θ on redetermination. It has recently been suggested [12] that non-bonded repulsion between the silicons in a dimer determines their distance of closest approach. For a Si-O distance of ~ 1.62 A, the Si-Si separation is ~ 3.08 A for $\theta = 144^0$. The Si-Si repulsion becomes severe when θ is reduced to $\sim 120^0$ (Si-Si separation ~ 2.8 A) and θ-values lower than this are thus practically ruled out.

The restrictions on the δ's will be essentially due to interactions between the neighboring oxygens. However, the closest separation observed between oxygens in most SiO_2 structures is much larger than the nonbonded contact separation between oxygens in a tetrahedron. Thus, restrictions due to non-bonded repulsions between oxygens is not likely to be an important factor in silica structure.

(c) <u>Ring Structures</u>

At this level of structural organization, we begin to see a possible multiplicity of rings constructed from the basic and dimer units. To build an N-membered oxygen ring, we start with tetrahedral unit 1, link it to unit 2 and link unit 2 to unit 3, etc., as in Fig. 15. If the (N + 1)th unit is the same as the first, then we have a closed ring of N bridging oxygens.

-16-

If it is not the same, then we have an open ring of N bridging oxygens. These rings have approximately equal sides which are equal to the edges of the basic tetrahedral unit (~ 2.65 A) and are a characteristic feature of silica structures, both crystalline and amorphous. In a sense, these rings sample the structure over a small domain and it is useful to describe silica structures in terms of the oxygen rings.

It is obvious that there should be consideable restrictions on the δ's in order to ensure ring closure and to ensure that the θ for the dimers of the ring are in the acceptable range. We have developed effective procedures by which one can identify the ranges in δ that lead to the formation of closed rings of different sizes and different geometries; i.e., containing 3,4,5 or 6 bridging oxygens. Although the three angular parameters θ, δ_1 and δ_2 were sufficient to describe the dimers, for the rings, one needs two sets of parameters: (1) those defining the geometry of the oxygen ring and (2) those defining the orientation of the constituent tetrahedra relative to the ring. We will first illustrate the use of these parameters with a 6-ring.

(1) The oxygens of a 6-ring are identified as 1,2,......6 and the sides 1-2, 2-3,....5-6, 6-1 are all roughly equal since they are an edge of a tetrahedron. the six angles at the vertices 1,2,......6 of the ring or, equivalently, the separation distances between alternate oxygens are needed parameters. These separations are between oxygens from adjacent tetrahedra forming a dimer. Three dihedral angles complete the set of parameters required to define the ring geometry. these dihedral angles could be equivalently described by the separations 1-4; 2-5 and 3-6. The geometry of the ring in α-quartz at a pressure of 68 Pa is shown in Fig. 16.

(2) The geometry of the ring, as define above, fixes only one edge of the six constituent tetrahedra. Assuming the tetrahedra to be regular, we

need only one other parameter to define the tetrahedra; i.e., a dihedral angle around the concerned edge with a chosen reference plane in the ring. This dihedral angle, which we shall call δ', can be used to define the corresponding Si which will automatically lead to a definition of the two remaining oxygens in the tetrahedron.

Using a different numbering scheme to identify the oxygens in Fig. 17, we will illustrate the procedure being used for classifying the ring structure of size 3,4,5 and 6. By varying the angles $\theta, \delta_1, \delta_2 \equiv \phi, \delta_1', \delta_2'$ for the dimer (Fig. 17a) over say $\theta \approx 120^0 - 180^0$, $\delta_1 \approx 0-180^0$ and $\delta_2 \approx 0-360^0$, all the O-O distances may be calculated between the two tetrahedra forming the dimer. In the complementary notation, the angle ϕ_1 at 1 is varied from 30^0 to 160^0. By using dihedral angles representing rotation about 1-2 and 1-3, with respect to plane 312 as reference, the silicons are located and the Si-Si distance in the dimer found. The dimer is now completey defined.

For each ϕ_1, the accepable Si-Si separation will place varying amounts of restriction on the δ''s and the distance 2-3 is known. Clearly, when 2-3 equals 1-2, we have a 3-oxygen ring. Considering Fig. 17b, the oxygen 4 is defined by ϕ_2 and a dihedral angle (3124). Similarly, oxygen 5 is defined by ϕ_3 and the dihedral angle (2135). When the distance 3-4 or 2-5 is zero, we have a 3-oxygen ring. When the distance of either of them is equal to the 1-2 distance, we have a 4-oxygen ring. When the distance 4-5 = distance 1-2, we have a 5-oxygen ring. When 4-5 = 2-3, we have a 6-oxygen ring and O_6 is defined by another dihedral angle around 5-4. In each case, our earlier study of the dimer will restrict the dihedral angle values because of the restriction of the range of the bridge angle (or of the Si-Si separation).

Although the results of these studies are not yet fully analyzed, we will briefly describe the trends that are appearing: (i) a 3-ring is highly

-18-

restricted in regard to all of its parameters. The ring angles should all be close to 60^0 since all the sides are nearly equal. the silicons should be located almost on the plane of the ring and outside of the ring to ensure adequate Si-Si separation (see Fig. 18). The bridge angles are about 130^0 in this case which is probably a strained configuration.

(ii) A 4-ring has a little more flexibility both with respect to ϕ_1 and the δ''s. The restriction on ϕ and δ', are even more relaxed in the cases of 5-rings and 6-rings. All such restrictions will be even more severe if the acceptable range in the bridge angles is less than the assumed range $(120^0\text{-}180^0]$.

(iii) It appears that dimer parameters leading to rings other than 6 are unlikely to exhibit long range order. However, formation of 6-rings does not necessarily imply long range order although most crystalline SiO_2 can be described in terms of 6-rings[1] with the ring geometry differing for different polymorphs.

(iv) The density of the structure is another factor in its acceptability. Rings like those in α-cristobalite may be found in the vitreous SiO_2 structure because the densities are similar whereas, rings close to those found in quartz can be ruled out for vitreous SiO_2 because of the much higher density for quartz.

(v) One other criterion still to be considered for the acceptibility of a stucture is the 0-0 separation. As mentioned earlier, all oxygens in crystalline silica have large enough separations that non-bonded repulsions are not a factor. The repulsive forces due to residual charges on the O's will ultimately decide the resultant geometry of the real structures. An analysis of the neighboring oxygen distances in crystalline SiO_2 will provide some clues in this regard. For example, the structure of α-quartz has been

determined at different pressures from 0.001 Pa to 68.0 Pa[3]. The results indicate that the tetrahedra suffer very little deformation and the compression is brought about mostly by the bending of the bridge angle,θ.

Over this pressure range, the Si-O distance changes from 1.615 A to 1.601 A; the Si-Si separation drops from 3.06 A to 2.95 A and θ changes from 142^U to 135^U . Looking at the smallest O-O distance in Fig. 5, it drops from 3.30 A to 2.84 A and it is seen that the closest oxygens are from second neighbor tetrahedra.

(2)   Modeling the Energetic Aspect of Interstitial Species in silica

In the present modeling of thermal oxidation of silicon, the emphasis has shifted from a parametric description to an atomistic description. At this new level of modeling we are confronted with a need for the following information: (i) solubility data for the various species, (ii) dissociation and ionization data for the various species within the SiO_2, (iii) bridging oxygen vacancy, V_0, and Frenkel defect, $V_0 + O_i$, formation energies, (iv) reaction energies for the internal oxidation of Si_I species to SiO, SiO_2, SiO_3 and (v) binding energies for the $V_0 - X_x$ pairs. In addition to needing this information for the bulk SiO_2, it is also needed for the non-stoichiometric interface blocking layer of SiO_2 which is thought to be so critical to the velocity of oxidation and to the formation of the fixed oxide charge, Q_f. This foregoing information is essential to an understanding of the mechanisms for (a) Q_f formation, (b) Cℓ adsorption, (c) Q_f annealing, and (d) network versus interstitial diffusion for various species. In addition, it is needed in order to determine the population of ionized versus neutral species so that a meaningful assessment may be made of electrical conduction in SiO_2 at oxidizing temperatures as well as of electric field effects on
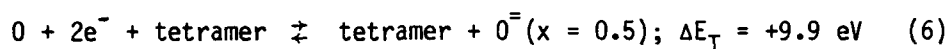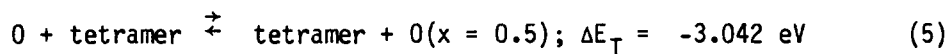
-20-

oxidation. Some portion of this information is accessable by experimentation; however, most of it is not and the only recourse we have is to theoretical computation. It is for this reason that we have used a molecular orbital approach to resolve these questions.

We have used the CNDO/2 method because the computation costs are considerably smaller than <u>ab initio</u> results[7,14]. Some limitations of our present method are that (i) the Si-O bond lengths are not optimized, for minimum total energies, (ii) the reaction energies are determined at 0^0K, (iii) these calculated energies are not absolute so that only relative energies between different species or conditions are likely to be relevant, (iv) we can only handle 82 orbitals and (v) we can only handle closed shell configurations. In our present method, we have adopted de Jong's [7] criteria that (1) all orbital energies of occupied MO's should be negative, (2) the total energy, E_T, should be minimized at a value of $\theta \sim 140^0$, (3) the binding energy of the molecule should be negative or close to zero and (4) bond overlap populations and other measures of bond energies should be consistent with geometries and dimensions observed in silicate structures.

In the previous report [1], we achieved the following results for O and Si interaction with a dimer unit and a tetramer ring:

$$O + H_6Si_2O_7 \rightleftharpoons H_6Si_2O_8 \ ; \quad \Delta E_T = -6.625 \text{ eV} \qquad (1)$$

$$O + 2e^- + H_6Si_2O_7 \rightleftharpoons H_6Si_2O_8^{2-} \ ; \ \Delta E_T = + 6.76 \text{ eV} \qquad (2)$$

$$Si + H_6Si_2O_7 \rightleftharpoons H_6Si_3O_7 \ ; \quad \Delta E_T = + 8.717 \text{ eV} \qquad (3)$$

$$Si + H_6Si_2O_7 \rightleftharpoons H_6Si_3O_7^{2+} + 2\bar{e} \ ; \quad \Delta E_T = + 19.2 \text{ eV} \qquad (4)$$

-21-
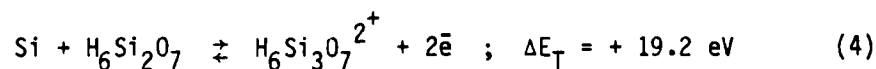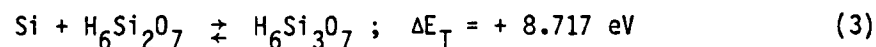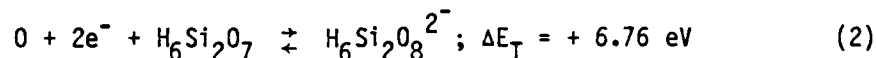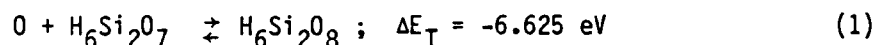
In the above equations, the electron work function was chosen as 5.1 eV. A larger value, by δE, would increase ΔE_T in Eqs. (2) and (4) by $2\delta E$. The following results with the tetramer ring ($H_8Si_4O_{12}$) were also achieved (with O_i at $x = 0.5$ Å)

$$0 + \text{tetramer} \overset{\rightarrow}{\leftarrow} \text{tetramer} + O(x = 0.5); \quad \Delta E_T = -3.042 \text{ eV} \qquad (5)$$

$$0 + 2e^- + \text{tetramer} \overset{\rightarrow}{\leftarrow} \text{tetramer} + O^=(x = 0.5); \quad \Delta E_T = +9.9 \text{ eV} \qquad (6)$$

$$0 + \text{tetramer} \overset{\rightarrow}{\leftarrow} \text{tetramer } O^{++} + 2e^-(x = 0.5); \quad \Delta E_T = +9.1 \text{ eV} \qquad (7)$$
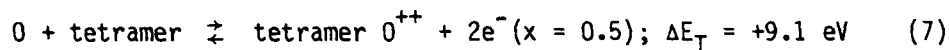
Again, the work function was chosen as 4.5 eV in Eqs. (6) and (7).

From Eqs. (1-7) we note that, if monatomic oxygen is available in the gas phase, it will be strongly absorbed by both the dimer and the tetramer. This conclusion also applies to $O^=$ (add - 9 eV to Eqs. (2) and (6)). However, ionization insitu to form $O^=$ is not a high probability event. The difference in energetics between the dimer calculation and the tetramer calculation is probably the same as that found by placing the O above versus below the bridging oxygen in the dimer. The reduced approach angle provides the enhanced repulsion force. This proposal will be tested shortly. Thus, the ΔE_T values given by Eqs. (1) and (5) apply to placing the O adjacent to the obtuse angle side versus the acute angle side respectively of a bridging oxygen in a ring interior to the SiO_2 volume. It is also very likely that the difference in these two values of ΔE_T is close to the activation energy for diffusion of the O species through a SiO_2 structure made from 4-membered rings; i.e., $Q_{Diff}^0 \approx 3.5$ eV, via the interstitial spaces.

-22-

The main question addressed during the present reporting period involved the interaction of O_2 and H_2O with the SiO_2 structure and whether or not dissociation is probable. First, we considered the O_2-tetramer reaction and found that the minimum energy condition involved the O_2 being placed at the center of the ring with the O-O bond being perpendicular to the plane of the ring and fixing its length to be that in O_2 at 25^0C. The following energetic reaction was observed

$$O_2 + \text{tetramer} \rightleftarrows (\text{tetramer} + O_2 \text{in center}); \Delta E_T = + 7.387 \text{ eV} \quad (8)$$
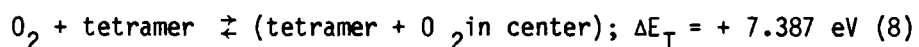
This, obviously, is not the energetically most favorable site in the SiO_2 volume, even though it is in the 4-ring, because it would lead to an impossibly small solid solubility for the O_2 compared to the experimental value of $\sim 10^{16}$ per cc at 1000^0C [15]. We shall see later that a much more favored site occurs on the outside of the 4-ring where the O_2 can approach the obtuse angle side of the bridging oxygen. For the moment, let us consider the dissociation of the O_2 in Eq. (8) to form 20, one of which enters an adjacent tetramer and both O's are located at 0.5 A from the center of its tetramer; i.e.,

$$O_2 + 2 \text{ tetramers} \rightleftarrows 2(\text{tetramer} + O(x=0.5)); \Delta E_T = +2.827 \text{ eV} \quad (9)$$
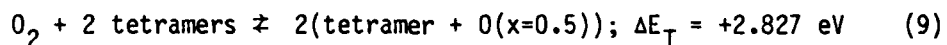
With this reaction we can expect a much greater solubility for O_2 in SiO_2 although ΔE_T is still too large. Perhaps with a 6-ring, the value of ΔE_T would be sufficiently reduced to match the experimental data (when entropy factors are also included).

When we turn to the interaction of O_2 with the dimers, a very interesting

-23-

result is obtained depending upon the orientation of the O_2 relative to the plane of the Si-O-Si atoms in the dimer. These results are illustrated in Fig. 19 where E_T is plotted as a function of the distance z between the bridging oxygen and the O-O line for two orientations of the O_2 molecule (a) in the Si-O-Si plane of the dimer and (b) perpendicular to the Si-O-Si plane of the dimer. In the former case, we have the reaction

$$O_2(p) + H_6Si_2O_7 \rightleftharpoons H_6Si_2O_9 \; ; \quad \Delta E_T \approx + 0.80 \text{ eV} \qquad (10)$$

and, from Fig. 1, we see that as Z is reduced from large values, there is a slight dip in ΔE_T and then an increase as z is reduced to ~ 1.21 A which is close to $d_{O-O} = 1.2074$ A . Turning to case (b), we note that if the $O_2(p)$ molecule rotates 90^u to the $O_2(b)$ position at $z \sim 1.95$ A, a second branch is available for E_T and this is a steeply descending branch (see Fig. 19). As z decreases and E_T descends along branch (b), the magnitude of the Si-O bridge bond decreases and reaches a zero value at $z \lesssim 1.36$ A and a minimum at z = 1.15 A . For this case the reaction equation is

$$O_2(\perp) + H_6Si_2O_7 \rightleftharpoons H_6Si_2O_9; \quad \Delta E_T \approx - 3.54 \text{ eV} \qquad (11)$$
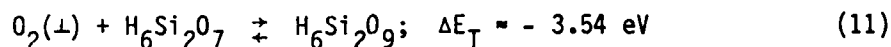
This is a bond breaking reaction which on the surface, appears to be a mechanism for vacancy formation at the bridging oxygen site. However, before we can be confident of the reality of this result, we must ascertain whether it is possible for the O_2 molecule to rotate by 90^u to form the $O_2(\perp)$ configuration within the volume of the SiO_2 or on the surface of the SiO_2 because of the hindrance of the basic tetrahedral units of the dimer at their normal dihedral angles, δ_1 and δ_2. Although it may be unlikely for this

-24-

normal dihedral angles, δ_1 and δ_2. Although it may be unlikely for this interesting event to take place in the volume of SiO_2, it is likely to occur on the surface of SiO_2.

In Fig. 20, the E_T values are given for the interaction of an H_2O molecule with the dimer unit for two configurations of the H_2O using $< HOH = 150°$ and $d_{O-H} = 0.96$ A. Only the (b) branch is a bond forming reaction. The following reaction equations apply to these two branches

$$H_2O(a) + H_6Si_2O_7 \rightleftharpoons H_8Si_2O_8(a); \quad \Delta E_T = + 1.42 \text{ eV} \tag{12}$$

$$H_2O(b) + H_6Si_2O_7 \rightleftharpoons H_8Si_2O_8(b); \quad \Delta E_T = -0.17 \text{ eV} \tag{13}$$
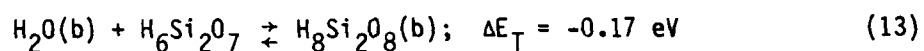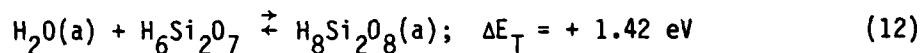
A third configuration (c) where a single H was bonded to the bridging oxygen was initially investigated by De Jong[7] who found

$$H_2O(c) + H_6Si_2O_7 \rightleftharpoons H_8Si_2O_8(c) ; \quad \Delta E_T = -0.35 \text{ eV} \tag{14}$$
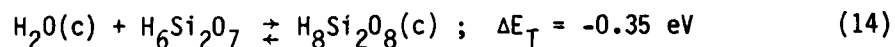
Once again, we would expect these three configurations to fit on the SiO_2 surface but there are real doubts that they would fit in the bulk SiO_2 without some repulsive energy contributions.

An additional reaction of H_2O with SiO_2 that can be simply assessed with the dimer is the dissociation reaction into H^+ and OH^-; i.e.,

$$H_2O + 2H_6Si_2O_7 \rightleftharpoons H_6Si_2O_7(H^+) + H_6Si_2O_7(OH^-); \quad \Delta E_T = +5.18 \text{ eV} \tag{15}$$
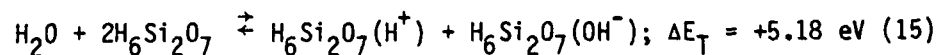
In Eq. (15), the H^+ and the OH^- are absorbed at the bridging oxygen sites at their minimum energy. This large positive energy change arises from the large

dissociation energy of H_2O into H^+ and OH^- since de Jong[7] found the following reactions

$$OH^- + H_6Si_2O_7 \rightleftarrows H_6Si_2O_7(OH^-); \quad \Delta E_T = -12.65 \text{ eV} \qquad (16)$$

$$H^+ + H_6Si_2O_7 \rightleftarrows H_6Si_2O_7(H^+); \quad \Delta E_T = -0.65 \text{ eV} \qquad (17)$$

It is the large difference in the binding energies of OH^- vs H^+ that leads to the strong negative surface charge of silica associated with the isoelectric point of ~ 2.0.

If we next consider the possible reactions of H_2O (-19.87 a.u.) with the tetramer unit (-236.5368 a.u.), we find the most favorable reaction is that given by configuration (g) in Fig. 21. Here, the 0 is in the center of the ring while the H's are above and below the ring directed towards an 0 unit of the tetramer ring. The reaction equation is

$$H_2O(g) + \text{tetramer} \rightleftarrows \text{tetramer } (+H_2O(g)); \quad \Delta E_T = +9.84 \text{ eV} \qquad (18)$$
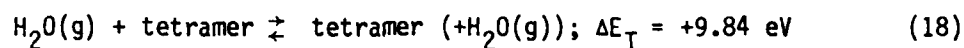
We also have the dissociation and ion binding reactions as

$$H_2O + 2 \text{ tetramers} \rightleftarrows \text{tetramer}(H^+) + \text{tetramer}(OH^-); \quad \Delta E_T = +16.28 \text{ eV} \quad (19)$$

$$H + \text{tetramer} \rightleftarrows \text{tetramer } (H^+) + e^-; \quad \Delta E_T = -10.28 \text{ eV} \qquad (20)$$

$$OH^- + \text{tetramer} \rightleftarrows \text{tetramer } (OH^-); \quad \Delta E_T = + 1.88 \text{ eV} \qquad (21)$$
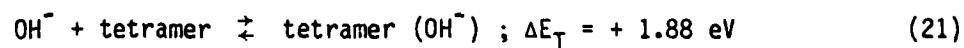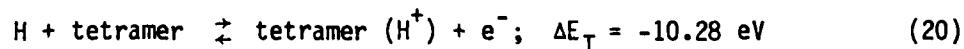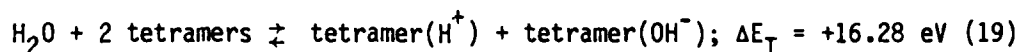
Once again, the large difference between Eq. (18) and the sum of Eqs. (19) and (20) is the dissociation energy of H_2O into H and OH. In Eq. (20), H is taken to have zero energy by convention.

From the foregoing, we can note that the calculations involving interactions with the dimer unit are (a) completely appropriate for SiO_2 surface in contact with the gas, (b) approximately correct for the bulk when we have a small interstitial species interacting with the obtuse angle of the bridging oxygen and (c) incorrect for the SiO_2 bulk when we have a large interstitial species interacting with the obtuse angle side of the bridging oxygen because of neglected interactions with the surrounding environment. The interactions with the tetramer ring give some insight into normal bulk SiO_2 interactions; however, we really need to treat the actual 6-ring to obtain final numbers. The tetramer calculations serve as a valuable and inexpensive learning tool. Tabulated formation energies for species interaction with the dimer and tetramer units are given in Table VI.

In closing this section, a word may be said concerning SiO_2 spectral information generated by the foregoing type of calculations. Although CNDO/2 calculations do not give the O(1S) core level energy, shifts in this energy level may be inferred from changes in the calculated gross atomic population of oxygen[16]. For example, from the calculated nearly neutral charge on the O_2 in the center of the tetramer, it can be inferred that the O(1S) spectrum from interstitial O_2 should be almost identical with that of molecular O_2. However, from the calculated charge on the bridging oxygen, the O(1S) core level shifts should be less than ~ 0.5 eV . Thus, a large solubility of O_2 molecules in SiO_2 may produce a shift to more negative energies (~ 13 eV) for the O(1S) photoemission spectrum.

TABLE I

SUMMARY OF EXPERIMENTS

ON

REACTIVE DEPOSITION OF ZnO_x, ZrO_x, AlO_x

Oxide Systems	Structure	ΔH_d(kcal)	ϕ
Si/0 yes	Amorphous	210	1.88
(ZnO) Zn/0 yes	Xtal (Hex)	166.8	1.59
(ZrO_2) Zr/0 yes	Xtal (Cubic)	259.5	1.56
α - Al/0 yes	Amorphous	266.8	1.28

$$\phi = \frac{V_A(MO_x)}{V_A(M)}$$

ΔH_d - Heat of decomposition (kcal)

TABLE II

SUMMARY OF EXPERIMENTS ON $A\ell O_x$ SYNTHESIS

	$A\ell$	Ar(torr)	O_2(torr)	Comments
194	500 ω (5.8 Å/sec)	4×10^{-3}	2×10^{-4}	$A\ell$, $A\ell O_x$
195	250 (3.2 Å/sec)	8×10^{-3}	1.6×10^{-4}	Oxidized target
196	400 (4-1 Å/sec)	8×10^{-3}	2×10^{-4}	Oxide (clear)
197	650 (7.0 Å/sec)	8×10^{-3}	2.2×10^{-4}	Oxide, $A\ell O_x$
198	650 (7.0 Å/sec)	8×10^{-3}	2.5×10^{-4}	Oxide, $A\ell O_x$
199	650 (7.0 Å/sec)	8×10^{-3} $O/A = 1.40$, $n_f = 20$	3.5×10^{-4}	$A\ell O_x$ $A\ell$ - 41.7 O - 58.3 } at%

TABLE III

EXPERIMENTAL PARAMETERS USED IN THE SYNTHESIS OF ZrO_x

Run	Zr(Power)	O_2(torr)	A_r(torr)	Comments
029	700 watts	2.7×10^{-4}	8×10^{-3}	Z_rO_2-Cubic
030	700	1.4×10^{-4}	8×10^{-3}	Z_rO_2-Cubic
031	700	7×10^{-5}	8×10^{-3}	Z_rO_2-Cubic

TABLE IV

EXPERIMENTAL PARAMETERS USED IN THE SYNTHESIS OF ZnO_x

Run	Z_n(Pwr)	O_2(torr)	A_r(torr)	Comments
022	150	6.5×10^{-4}	8×10^{-3}	target oxidized
023	300	6.5×10^{-4}	8×10^{-3}	reduced ZnO_x
024	250	5.7×10^{-4}	8×10^{-3}	reduced ZnO_x
025	250	6.5×10^{-4}	8×10^{-3}	ZnO
026	250	6.5×10^{-4}	8×10^{-3}	ZnO

TABLE V

HIGHLIGHTS OF SiC DEPOSITIONS

Temperature	Film/Substrate	X-ray Analysis
25°C	SiC/Si	amorphous
700°C	SiC/Al$_2$O$_3$	β SiC 111 reflection "preferred orientation"
750°C	SiC/Si	β SiC 111 reflection
830°C	SiC/Si	β SiC 111 reflection

TABLE VI

INTERACTION ENERGIES FOR INTERSTITIAL SPECIES INTERACTIONS
WITH DIMER (D) AND TETRAMER (T)

Species	Dimer ΔE_T^D (eV)	Tetramer ΔE_T^T (eV)
Si^0	+ 8.72	
Si^{++}	+19.2	
0	- 6.63	- 3.04
$0^=$	+ 6.76	+ 9.9
0^{++}		+ 9.1
$O_2(p)$	+ 0.80	
$O_2(\perp)$	- 3.54	+ 7.4
$O_2 + 2T \rightleftharpoons 2(T+0)$		+ 2.83
$H_2O(a)$	+ 1.42	
$H_2O(b)$	- 0.17	
$H_2O(c)$	- 0.35	
$H_2O(g)$		+ 9.84
H^+	- 0.65	-10.28
OH^-	-12.65	+ 1.88
$H_2O + 2T \rightleftharpoons TH^+ + TOH^-$	+ 5.18	+16.28

REFERENCES

1. W. A. Tiller and T. W. Barbee, Jr., "Fabrication and Properties of Multilayer Structures." Second Semiannual Technical Report for Period 1 March 1980 - 30 August 1980, ARPA.

2. G. Neumann and G. M. Neumann, Surface Self-Diffusion of Metals, Diffusion Monograph Series, Ed: F. H. Wöhlbier, 1972, No. 1.

3. W. A. Tiller, "On the Kinetics of the Thermal Oxidation of Silicon, Part I: A Theoretical Perspective," J. Electrochem. Soc. 127, no. 3, 619-624 (1980).

4. W. A. Tiller, "On the Kinetics of the Thermal Oxidation of Silicon, Part II: Some Theoretical Evaluation," J. of Electrochem. Soc., 127. no. 3, 625-632 (1980).

5. W. A. Tiller, "On the Kinetics of the Thermal Oxidation of Silicon, Part III: Coupling with Other Key Phenomena," J. Electrochem. Soc. 128, no. 3, 689-694 (1981).

6. R. A. Robie, B. S. Hemingway and J. R. Fisher, "Thermodynamic Properties of Minerals," U.S.G.S. Bulletin, p 1452 (1978).

7. B. H. W. S. de Jong, "A Spectroscopic and Molecular Orbital Study on the Polymerization of Silicate and Aluminate Tetrahedra in Aluminosilicate Metals, Glasses and Aqueous Solutions," Ph.D. Thesis, Stanford University, December 1980.

8. K. Hubner, "Chemical Bond and Related Properties of SiO_2," Phys. Stat. Sol. 40, 487-495 (1977).

9. R. J. Bell and P. Dean, "Structure of Vitreous Silica - Validity of Random Network Theory, Phil. Mag. 25, 1381-1398 (1972).

10. A. F. Wright and A. J. Leadbetter, "Structure of Beta Cristobalite Phases of SiO_2 and $A\ell PO_4$," Phil. Mag. 31, 1391-1401 (1975).

11. D. R. Peacor, "High Temperature Single Crystal Study of Cristobalite Inversion," Z. Kristallog 138, 274-298 (1973).

12. C. Glidwell, "Cation-Cation Distances in Polymorphs of Silica and Their Analogs," Inorg. Nucl. Chem. Lett. 13, 65-68 (1977).

13. Y. Le Page and G. Downay, "Refinement of Crystal Structure of Low Quartz," Acta Cryst. B32, 2456-59

14. M. D. Newton and G. V. Gibbs, "Ab Initio Calculated Geometries and Charge Distributions for H_4SiO_4 and $H_6Si_2O_7$ Compared with Experimental Values for Silicates and Siloxanes," Phys. Chem. Minerals 6, 221-246 (1980).

15. F. J. Norton, Nature 171, 701 (1961).

16. P. S. Bagus, "Core Binding-Energy Shifts for Free Negative Ions of Oxygen: O^0 to O^{2-}," J. Electron Spectroscopy and Related Phenomena 20, 183-190 (1980).

FIGURE CAPTIONS

1. (a) Schematic diagram of new sputtering chamber. (b) Schematic of new gas dispersion ring.

2. Comparison of our refractive index vs. stoichiometry data with the SIPOS data.

3. Controlling P_{O_2} values to produce a given film stoichiometry (x in SiO_x) for several sputtering power levels.

4. Variation of index of refraction, η, and film thickness, t_f, as a function of radial distance from the edge of the wafer for a $SiO_{1.5}$ film.

5. Plot of O/Aℓ ratio in $A\ell O_x$ film as a function of radial distance from the center of the wafer for sample 197 (Aℓ - 650 watts, O_2 - 2.2×10^{-4} torr, Ar - 8×10^{-3} torr, and 7.0 Å/sec deposition rate).

6. Plot of electrical resistance as a function of radial distance for ZnO_x film (sample 81-024).

7. Schematic illustration of our two-source deposition system for SiC_x film formation (SC silicon and graphite sources, 4 micron Ar pressure, 25^oC - 830^oC substrate temperature, and (100) Si or ($1\bar{1}02$) $A\ell_2O_3$ substrates).

8. Variation of C and Si concentration, evaluated via electron microscopy, with distance along the SiC_x film for two different deposition power levels for the Si (250 W and 500 W).

9. Log transmitted intensity as a function of wavelength to measure the SiC bandgap.

10. Schematic illustration of Sn liquid-like film effect on the deposition of SiC.

11. Temperature dependence of surface diffusion coefficient of Cu, D_s, at several different values of Pb vapor pressure. (Adapted from Fig. 16 and Fig. 26 of Ref. 2.)

12. Basic structural unit in SiO_2: oxygen tretrahedron plus silicon interstitial. The tetrahedron is almost regular (4 Si-O distances $\approx$ 1.62 ± 0.05 $\overset{o}{A}$; 6 O-O distances $\approx$ 2.65 ± 0.10 $\overset{o}{A}$, and O-Si-O angles $\approx$ 110° ± 10°).

13. Scheme for linking tetrahedra: 1 is the starting unit, 2-5 are first neighbors of 1 and 6-17 are second neighbors of 1. Three angular parameters define the relative orientations of the linking tetrahedra.

14. (a) Drawing of a tetrahedra dimer: angles θ, δ_1 and δ_2 fully define the dimer. (b) The dihedral angle, δ_1, (the distance $Si_2 - O_1$ is a measure of δ_1).

15. Scheme used for the formation of closed rings.

16. Illustration of key angles and distances in the 6-ring of α-quartz at 68 P_A (distance 2-5 is 4.89 $\overset{o}{A}$ and 3-6 is 4.94 $\overset{o}{A}$). At 0.001 P_A, the distance 1-4 is 3.30 $\overset{o}{A}$.

17. (a) Classification of the dimer structure via the angles ϕ_1, δ_1', $\delta_2' \equiv \theta$, δ_1, δ_2. (b) Specification of oxygen locations 4 and 5 in a ring relative to the dimer via bond angles ϕ_2 and ϕ_3, plus dihedral angles (3124) and (2135). Restrictions on δ' for $\theta > 120^o$.

18. A 3-oxygen ring with the silicons in the plane of the ring illustrating almost total constraint of the δ''s. (b) A 4-oxygen ring with $\theta \approx 160^o$ for Si_1 and Si_2. Here, $\delta'(Si_i) \sim 0$ to 40°, and $\delta'(Si_2) \sim 160^o$ ± 20°.

19. Interaction energy, E_T, of O_2 with the dimer as a function of separation distance, Z; (a) non-bonding reaction (O_2 in plane of Si-O-Si), (b) bonding reaction (O_2 perpendicular to plane of Si-O-Si).

20. Interaction energy, E_T, of H_2O with the dimer as a function of separation distance, Z; (a) non-bonding reaction (H_2O perpendicular to the plane of Si-O-Si), (b) bonding reaction (HO in-plane and H perpendicular to the plane of Si-O-Si).

21. Interaction energy, E_T, of H_2O with the tetramer for a number of different H_2O configurations in the ring. Configuration (g) is the most favorable (H-O-H angle = 105° in all cases).

FIGURE 1(a)

TARGET →

Ar →

O_2
SUBSTRATE
HEATER →

CRYO
PUMP

-39-
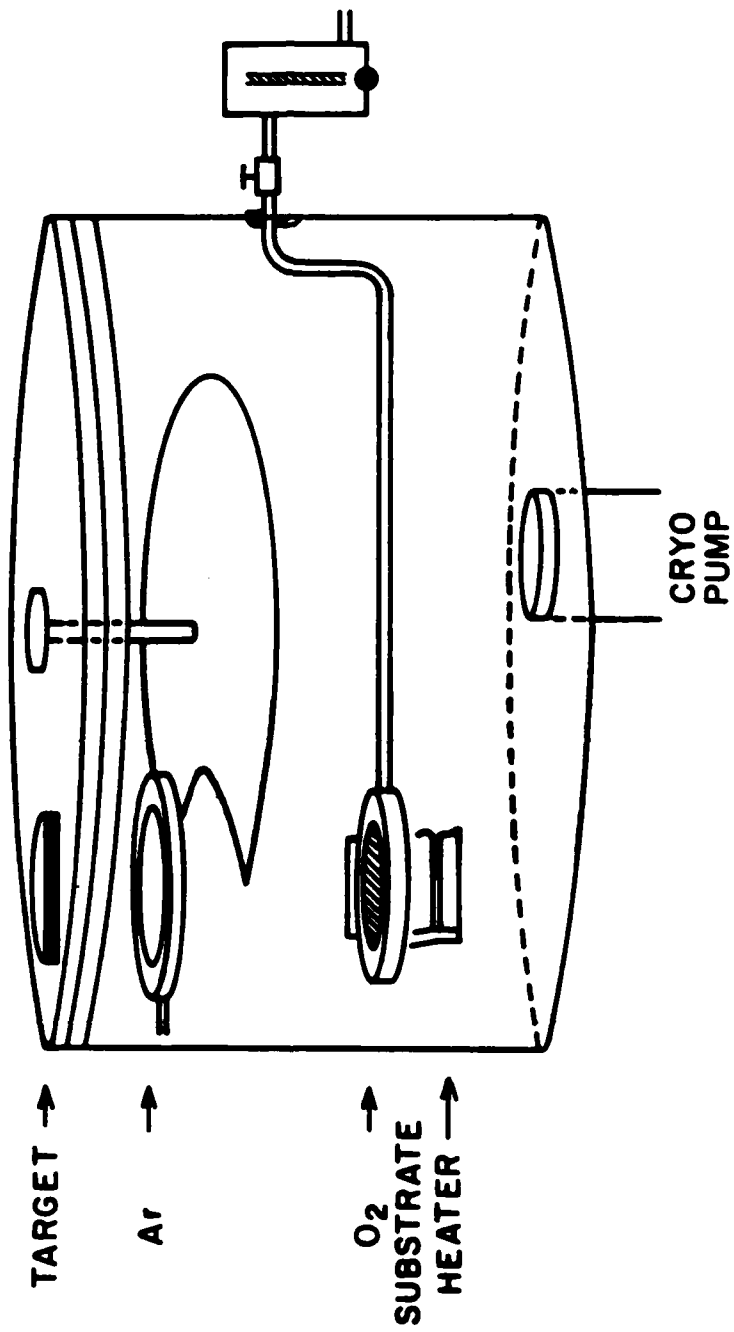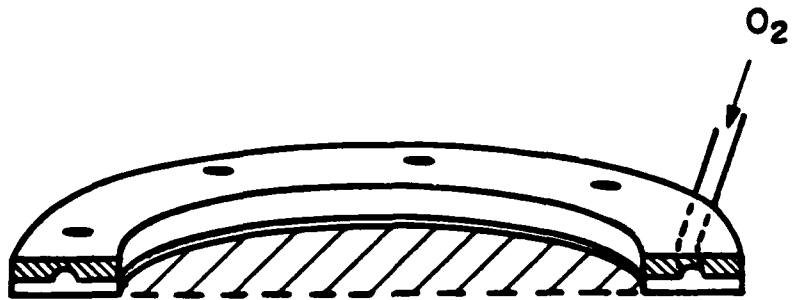
GAS DISPERSION RING

FIGURE 1(b)
-40-
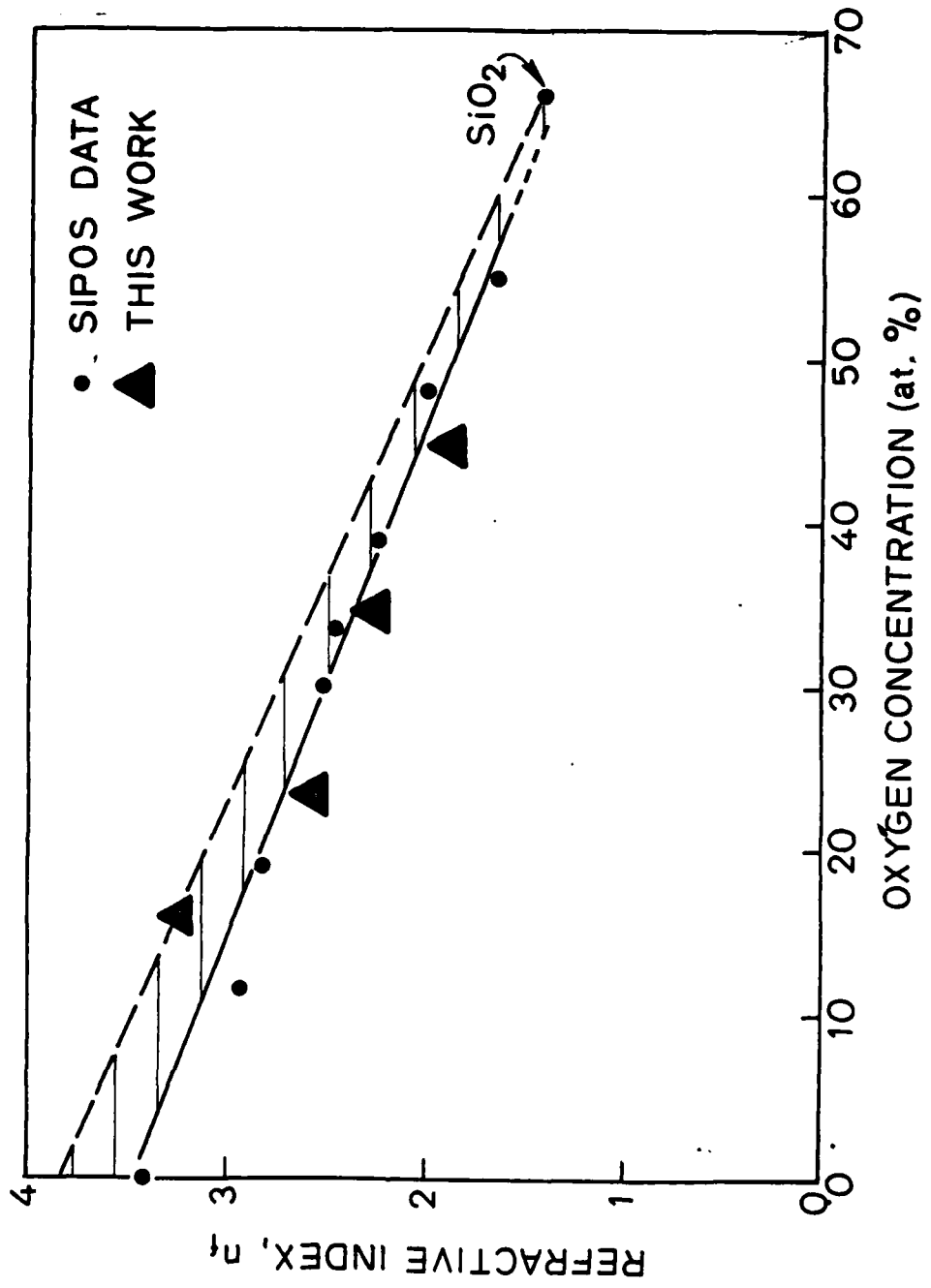
FIGURE 2

-41-

FIGURE 3

VALUE FOR 'X' IN SiO$_X$

PO$_2$ μM

700 ω

500 ω

300 ω

FIGURE 4
-43-

FIGURE 5

-44-

FIGURE 6

-45-

FIGURE 7

-46-

FIGURE 8

-47-

FIGURE 9

-46-
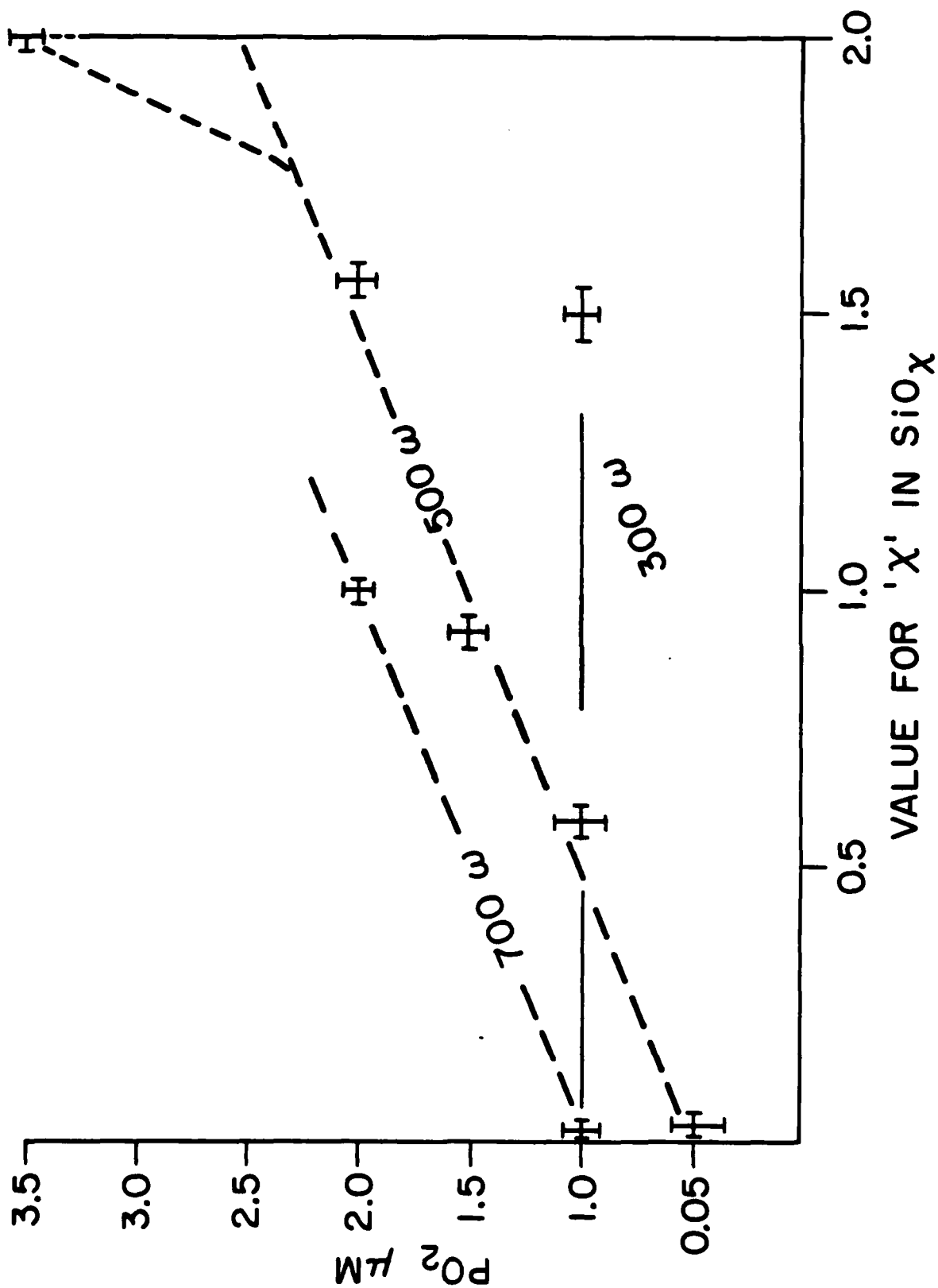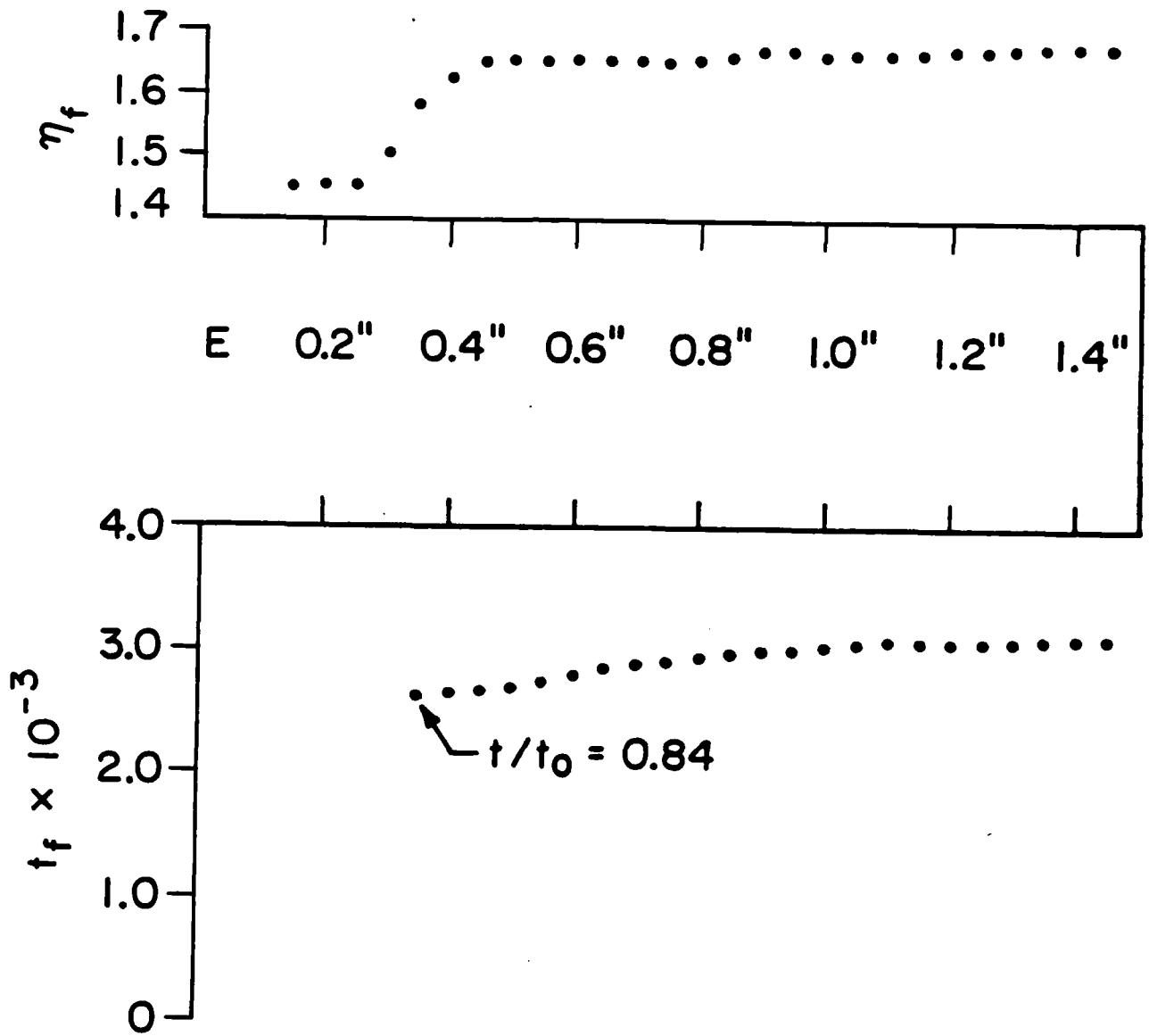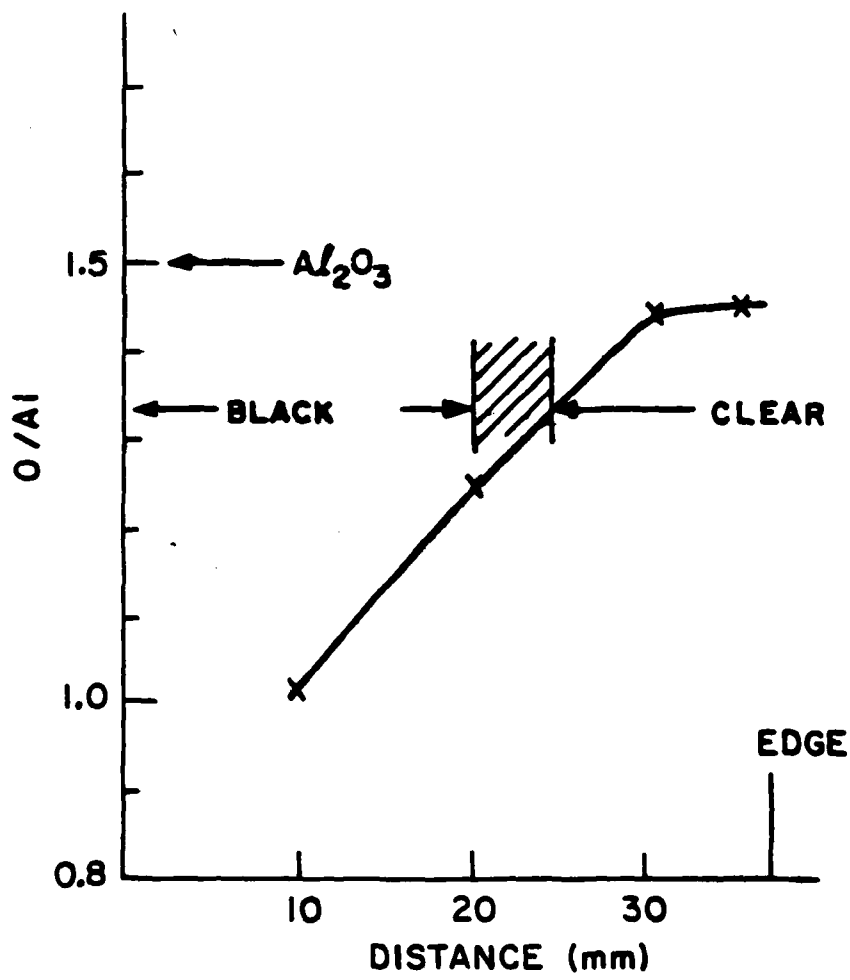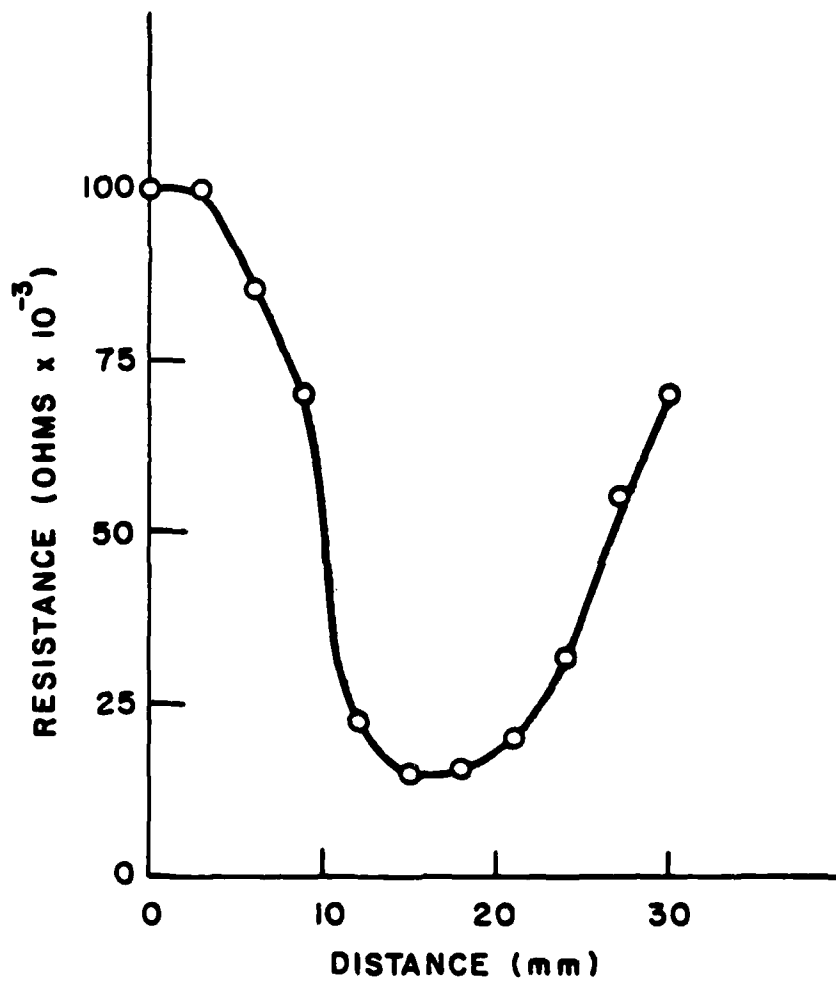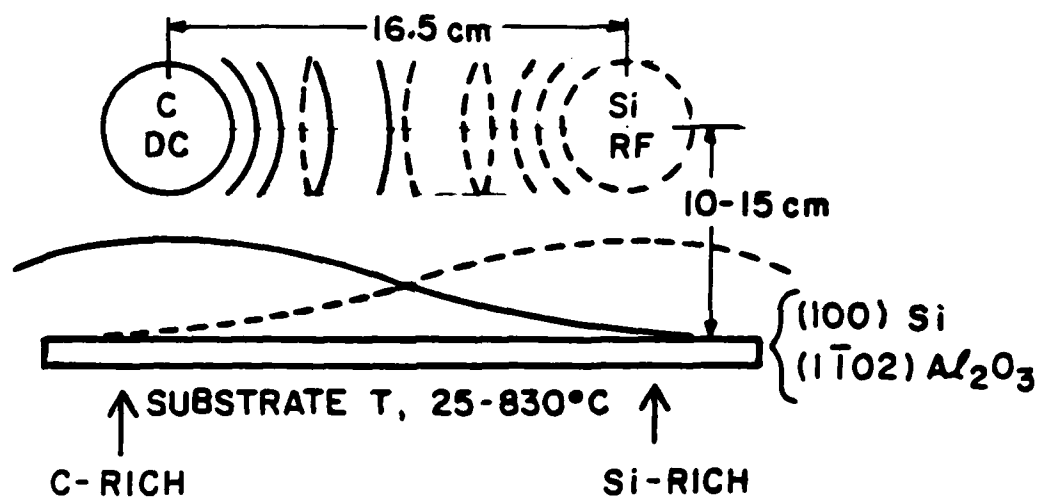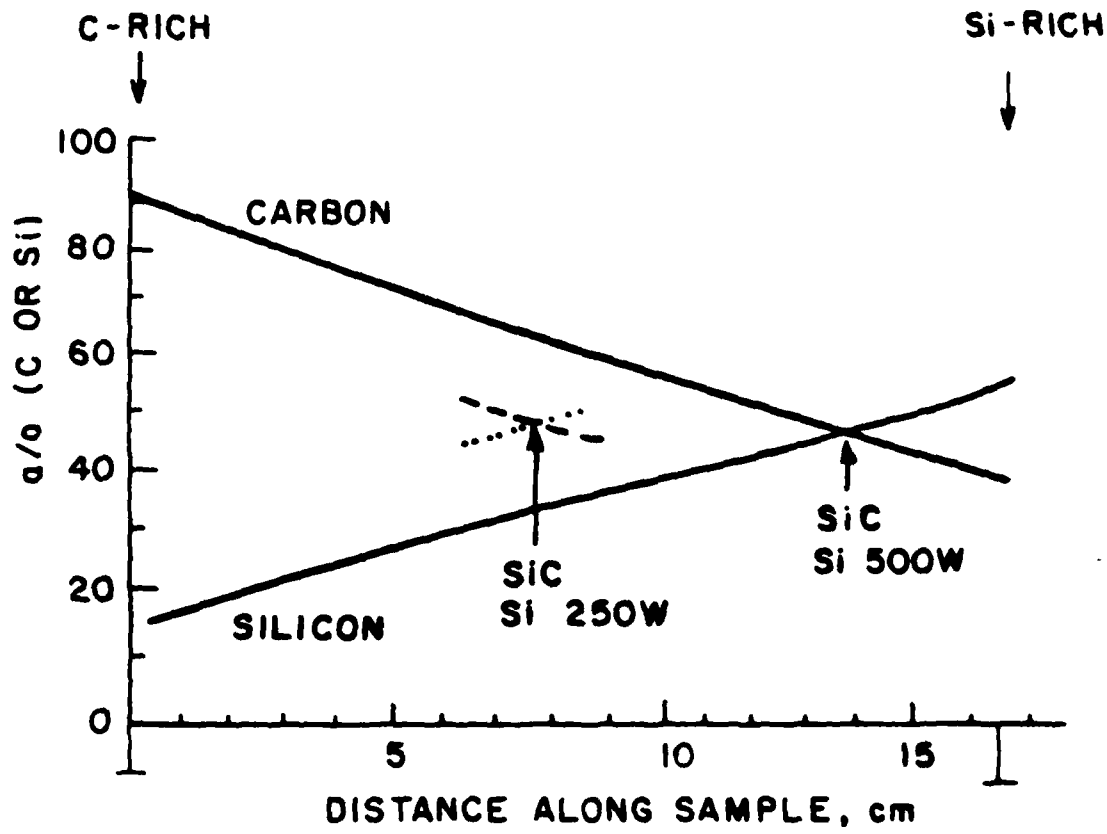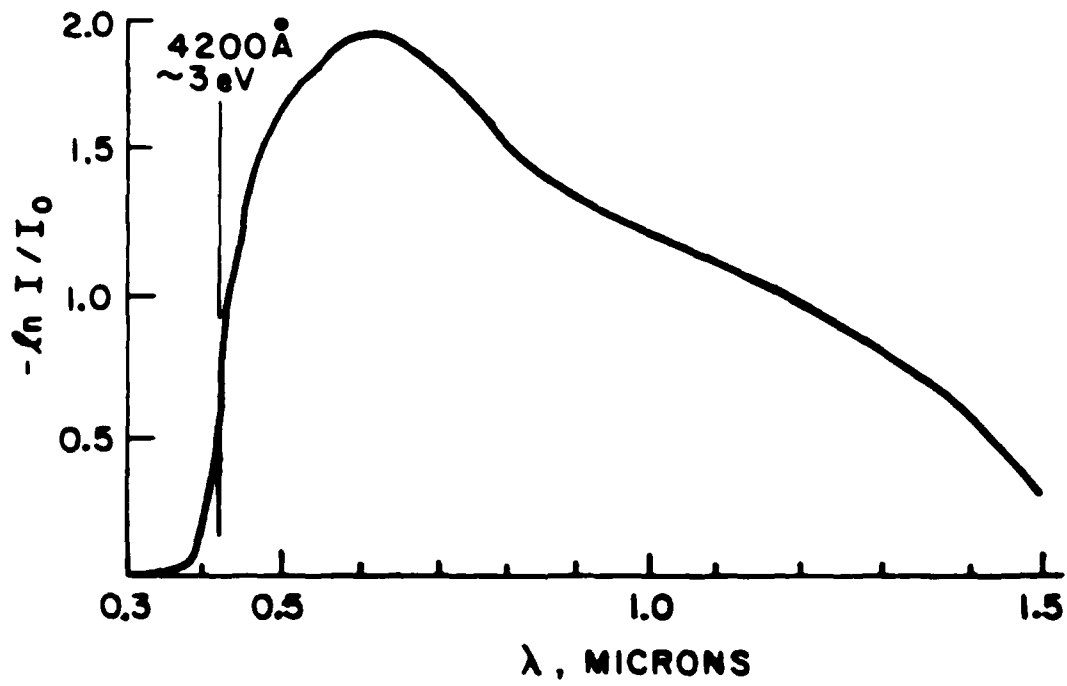
LIQUID-LIKE FILM EXAMPLE
SiC DEPOSITION WITH Sn
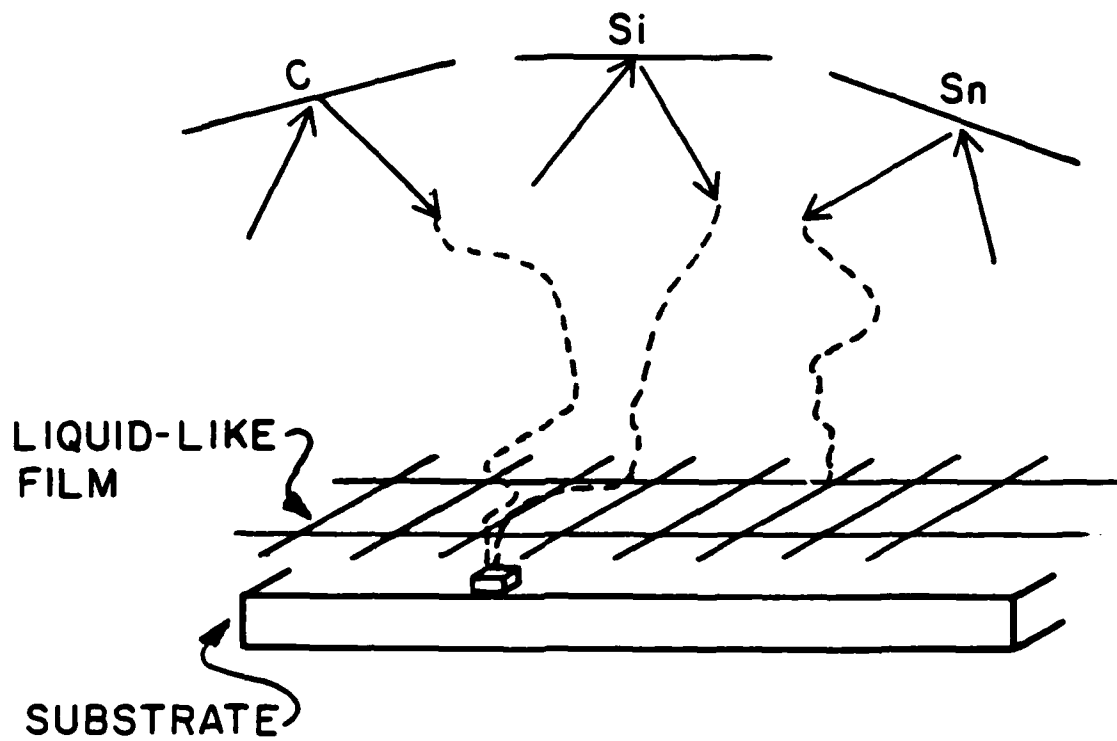
FIGURE 10

FIGURE 11
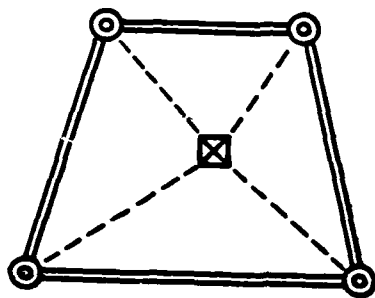
-50-

◉ OXYGEN

⊠ SILICON

FIGURE 12

FIGURE 13

-52-

FIGURE 14

-53-

DIMER PARAMETER
REPRESENTATION

TETRAHEDRON

CONNECTING OXYGENS
OF CLOSED RINGS

FIGURE 15

-54-

FIGURE 16

-55-

FIGURE 17

(a)

(b)
FIGURE 18   -57-

FIGURE 19

$d_{0-0} = 1.2074 \text{Å}^\circ$

z (Å)

E_T (a.u.)

(a)

(b)

∠H-O-H = 105°
d_{O-H} = 0.96A°

z

H H
H··O
  Si Si

(a)

O··H
H
Si Si

(b)

-157.8550
-157.8600
-157.8650
-157.8600
-157.8750
-157.8800
-157.8850
-157.8900

E_T (a.u.)

1.4 1.5 1.6 1.7 1.8 1.9 2.0 2.1 2.2 2.3

z (Å)
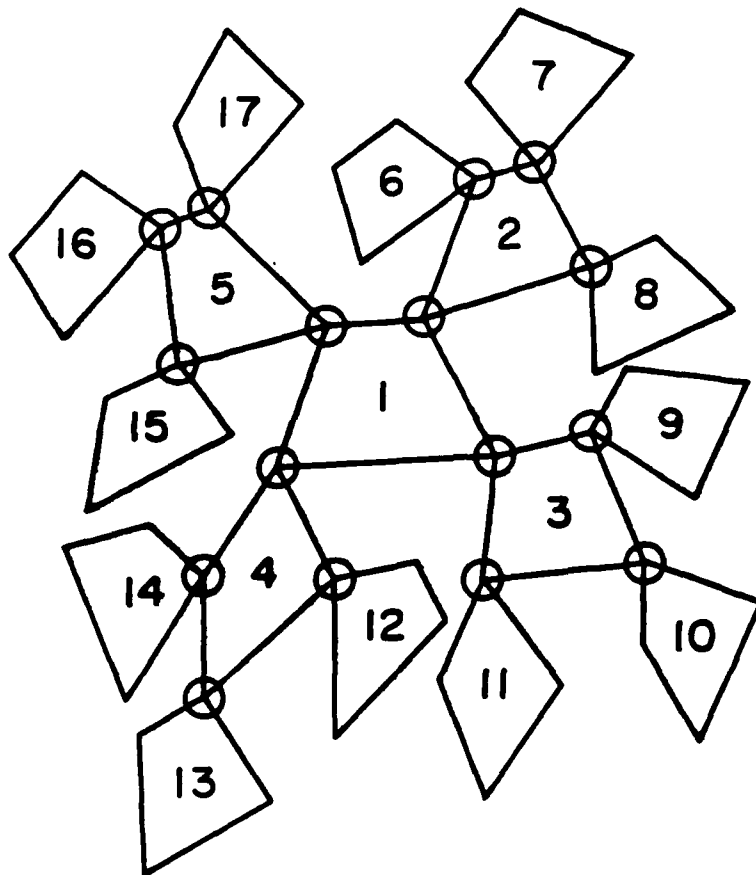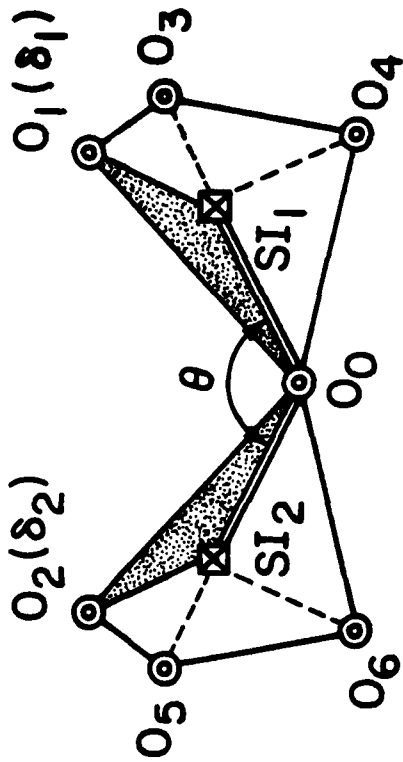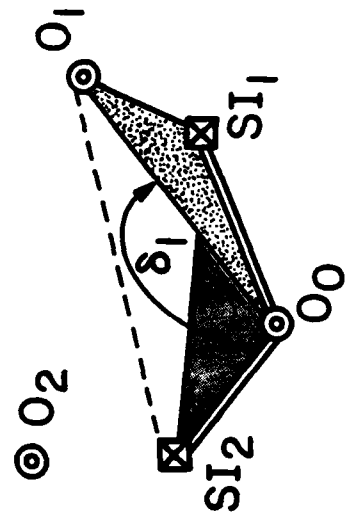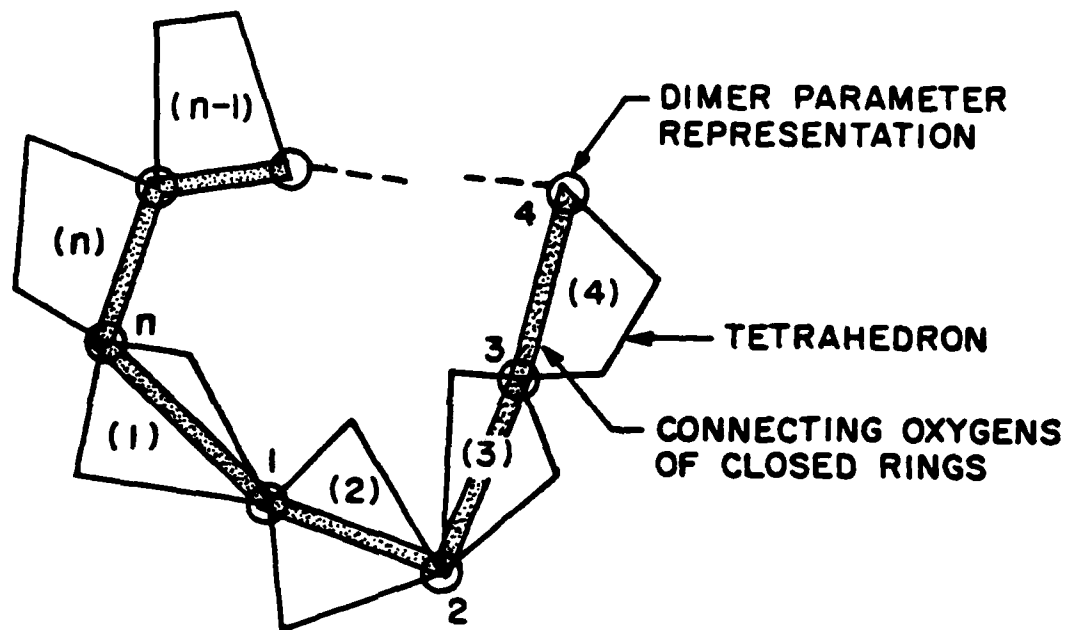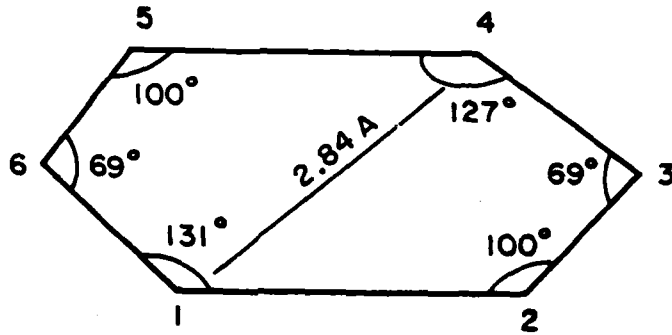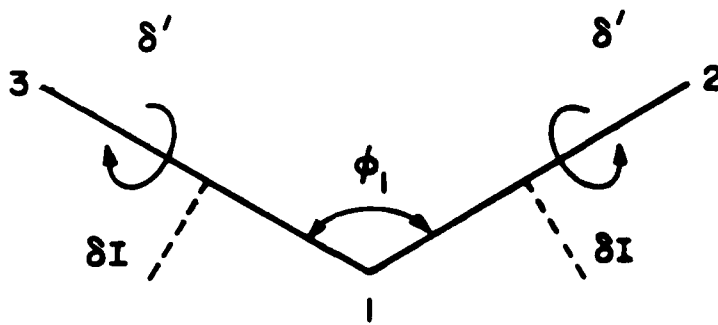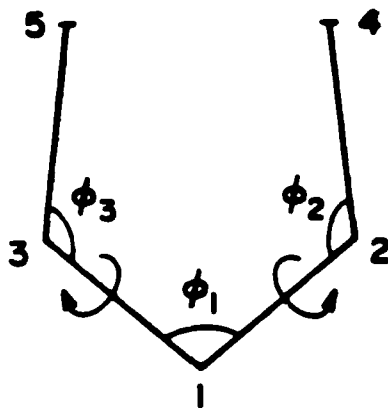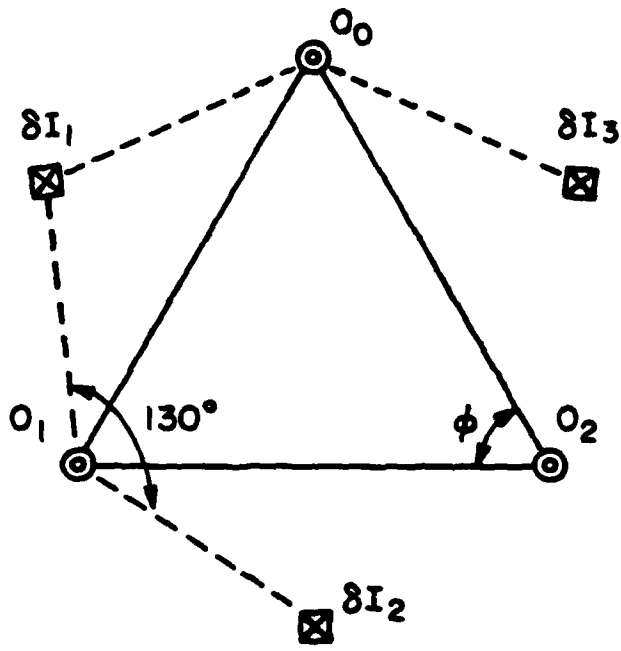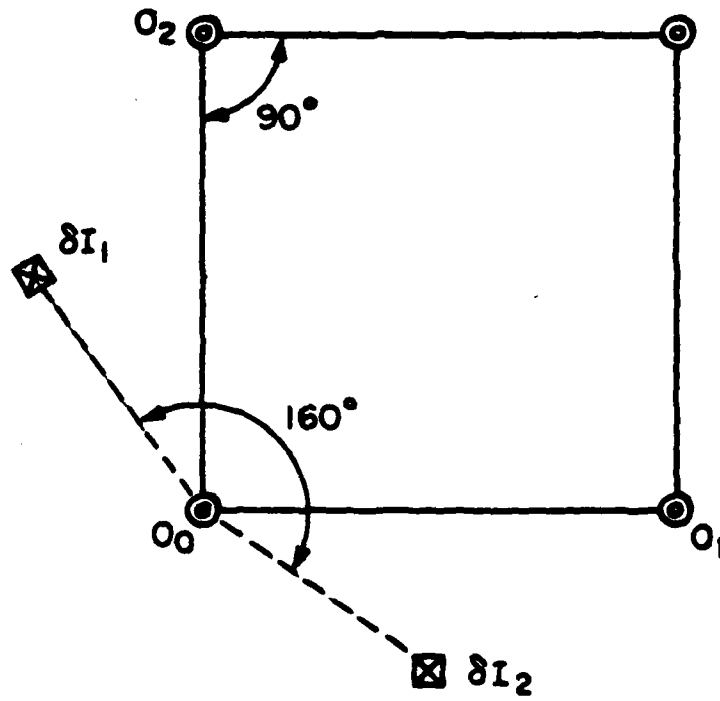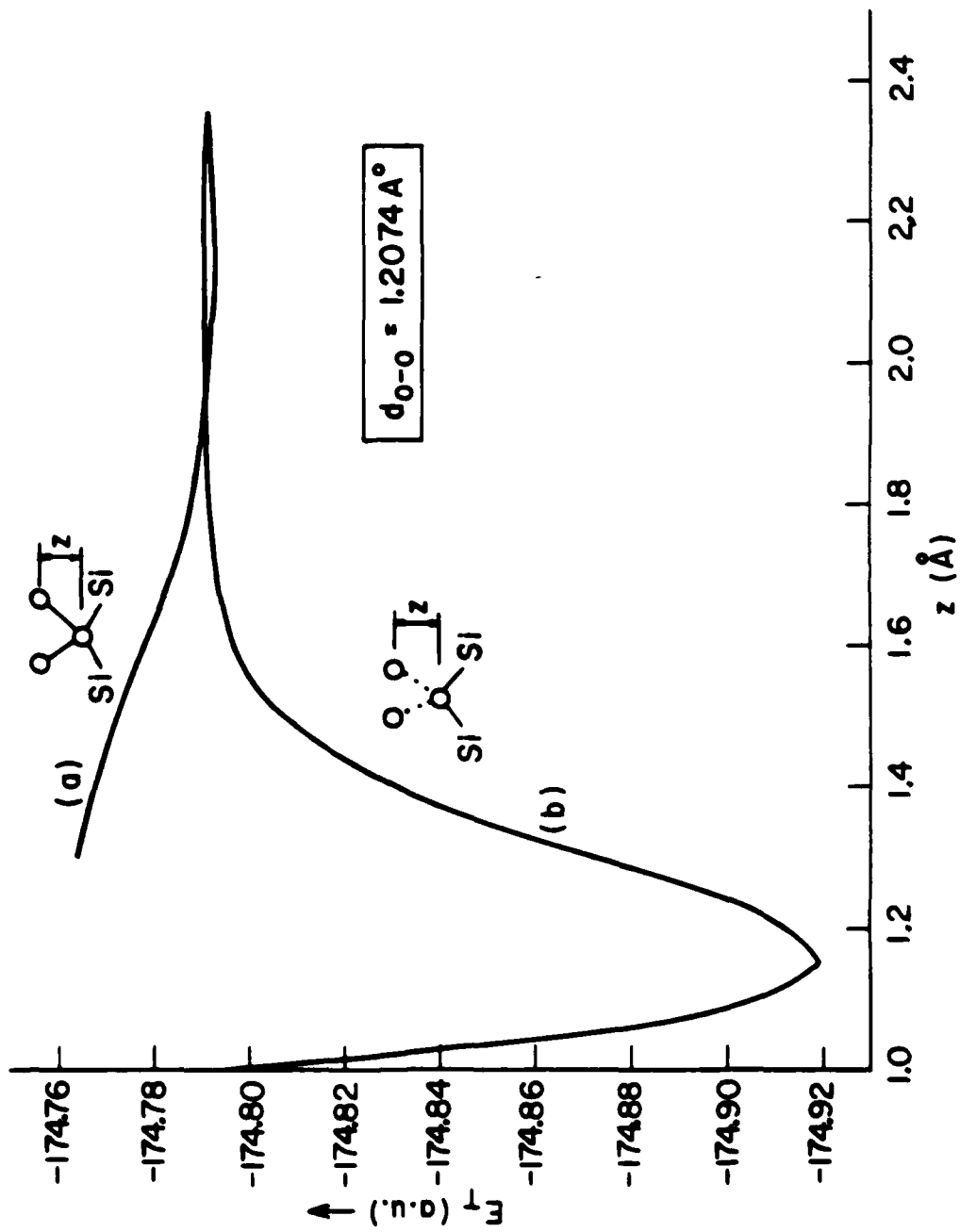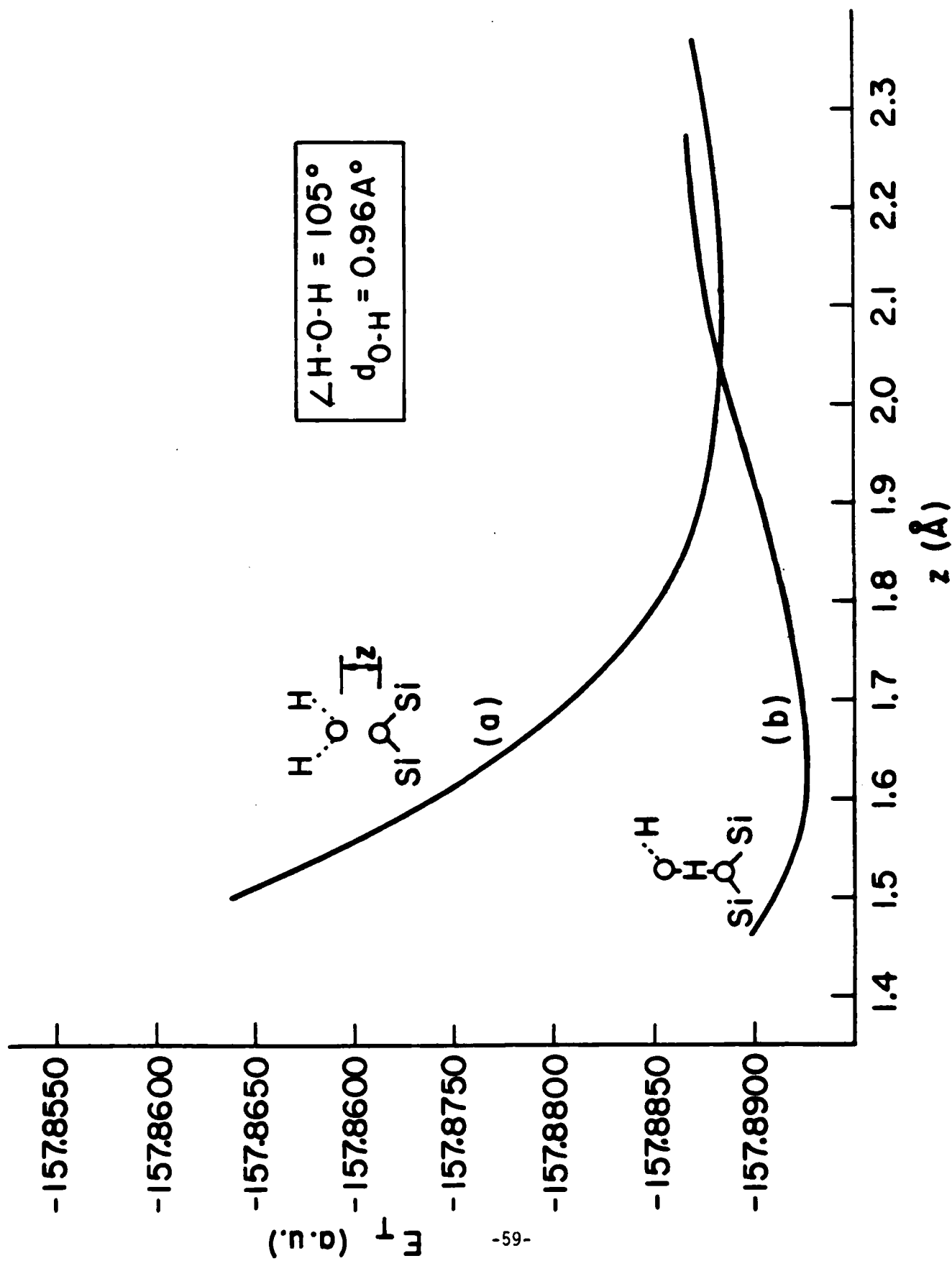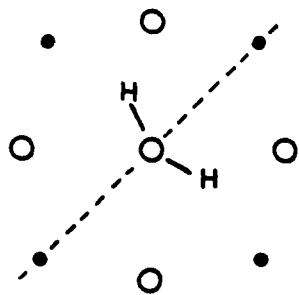
FIGURE 20

$E_T = -255.4846 \, (\text{a.u.})$

(a)
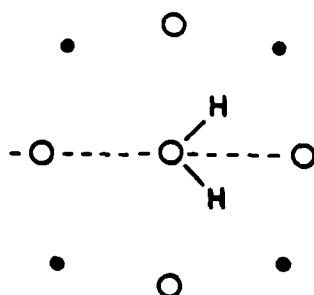
$E_T = -255.5766 \, (\text{a.u.})$

(b)
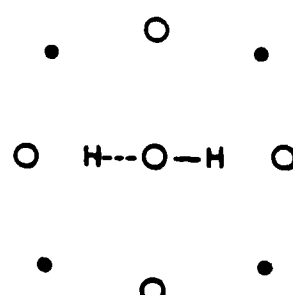
$E_T = -255.7822 \, (\text{a.u.})$

(c)
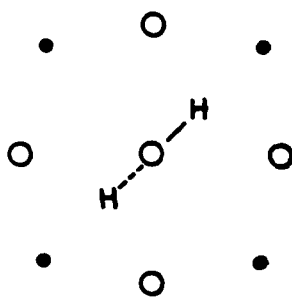
$E_T = -255.8451 \, (\text{a.u.})$

(d)
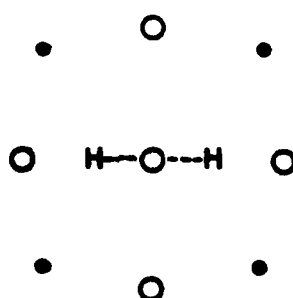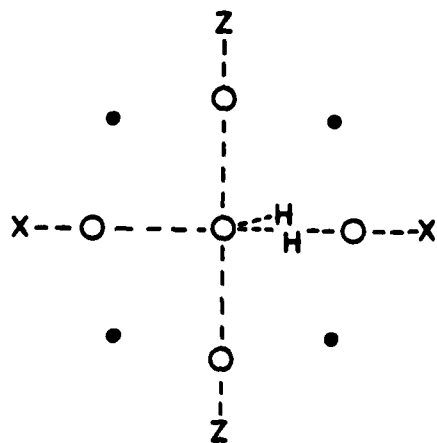
$E_T = -255.9430 \, (\text{a.u.})$

(e)
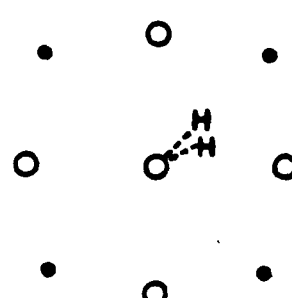
$E_T = -256.0353 \, (\text{a.u.})$
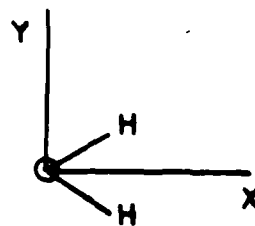
(f)

$E_T = -256.0450 \, (\text{a.u.})$

(g)

FIGURE 21